analgesics. Acute back pain can decrease patient quality of life (QOL) [11]. This reduction in back pain with a shorter period of bed rest is considered to improve QOL and to relieve some of the discomfort associated with renal biopsy. Prolonged bed rest after diagnostic procedures is not always safe and may impose an increased burden on patients [12]. In fact, prolonged bed rest after renal biopsy may have adverse consequences, such as pulmonary embolism [10].

Concern has been expressed that shorter periods of bed rest may increase serious complications such as bleeding. To prevent serious complications after renal biopsy, 24 h of enforced bed rest has commonly been recommended. However, same-day renal biopsy with a shorter period of bed rest has also been advocated. Some recommend 6 h of bed rest after renal biopsy, citing the fact that serious bleeding complications usually occur within 6 h, and that perinephric hematoma size is usually smaller at 24 h than at 6 h post biopsy [13]. The safety of same-day renal biopsy after 4–6 of strict bed rest has also been reported [4–7]. In addition, in a study of bed rest after liver biopsy [14], no difference in the incidence of bleeding complications between 6 and 24 h of strict bed rest was reported.

Our study showed no significant differences between 2 and 7 h of strict bed rest with respect to serious bleeding complications or progression of anemia after biopsy. Our findings suggest that shortening the period of strict bed rest to 2 h after renal biopsy is safe. However, we must emphasize that the total period of bed rest after biopsy in all cases was about 18 h, so our results do not reflect early discontinuation of all bed rest. In Japan, standard postbiopsy care includes compression of the biopsy site with sand bags or an abdominal bandage [9], yet the rationale for such care has not been reported. Based on our observations, an abdominal compression bandage may be unnecessary.

If a large perinephric hematoma forms after renal biopsy, most patients will complain of back pain, which is difficult to distinguish from the pain due to strict bed rest. Thus, a reduction in back pain due to enforced bed rest may be helpful in early detection of severe perinephric hematoma.

Furthermore, shortening the period of bed rest after biopsy can reduce hospitalization time, ultimately leading to a decrease in medical costs. On the other hand, it should be noted that early discontinuation of strict bed rest may have resulted in poor compliance with bed rest in young male patients.

Study limitations

This observational study is retrospective, so the extent of complications during the study period may have been underestimated. This point was considered in defining back pain requiring analgesics as the primary outcome in an effort to minimize differences in identifying back pain during the study observation period. During the period of 2 h strict bed rest, two patients required blood transfusions. Although not statistically significant, this potentially serious complication, even in a single patient, is clinically important. Therefore, bed rest recommendations after renal biopsy require further careful investigation.

Conclusions

Shortening the period of strict bed rest after renal biopsy from 7 to 2 h decreased the incidence of back pain, but there was no increase in bleeding or other biopsy-related complications. Our findings suggest that a shorter period of strict bed rest can safely reduce discomfort in renal biopsy patients.

References

1. Iversen P, Brun C. Aspiration biopsy of the kidney. Am J Med. 1951;11:324–30.
2. Madaio MP. Renal biopsy. Kidney Int. 1990;38:529–43.
3. Kim D, Kim H, Shin G, Ku S, Ma K, Shin S, et al. A randomized, prospective, comparative study of manual and automated renal biopsies. Am J Kidney Dis. 1998;32:426–31.
4. Fraser IR, Fairley KF. Renal biopsy as an outpatient procedure. Am J Kidney Dis. 1995;25:876–8.
5. Simckes AM, Blowey DL, Gyves KM, Alon US. Success and safety of same-day kidney biopsy in children and adolescents. Pediatr Nephrol. 2000;14:946–52.
6. Lin WC, Yang Y, Wen YK, Chang CC. Outpatient versus inpatient renal biopsy: a retrospective study. Clin Nephrol. 2006; 66:17–24.
7. Al-Hweish AK, Abdul-Rehaman IS. Outpatient percutaneous renal biopsy in adult patients. Saudi J Kidney Dis Transpl. 2007;18:541–6.
8. Whittier WL, Korbet SM. Timing of complications in percutaneous renal biopsy. J Am Soc Nephrol. 2004;15:142–7.
9. Nishi S. Prescription of bed-rest after renal biopsy. Nippon Jinzo Gakkai Shi. 2005;47:491–6.
10. Ishikawa E, Nomura S, Hamaguchi T, Obe T, Inoue-Kiyohara M, Oosugi K, et al. Ultrasonography as a predictor of overt bleeding after renal biopsy. Clin Exp Nephrol. 2009 [Epub ahead of print]
11. Coste J, Lefrancois G, Guillemin F, Pouchot J. Prognosis and quality of life in patients with acute low back pain: insights from a comprehensive inception cohort study. Arthritis Rheum. 2004;51:168–76.
12. Allen C, Glasziou P, Del Mar C. Bed rest: a potentially harmful treatment needing more careful evaluation. Lancet. 1999; 354:1229–33.
13. Jones B, Puvaneswary M, Nanra R, Trevillian P, Carney S, Gillies A. Reduced duration of bed rest after percutaneous renal biopsy. Clin Nephrol. 1991;35:44–5.
14. Minuk GY, Sutherland LR, Wiseman DA, MacDonald FR, Ding DL. Prospective study of the incidence of ultrasound-detected intrahepatic and subcapsular hematomas in patients randomized to 6 or 24 hours of bed rest after percutaneous liver biopsy. Gastroenterology. 1987;92:290–3.

NDT

Nephrology Dialysis Transplantation

Original Article

Glomerular and proximal tubule cysts as early manifestations of *Pkd1* deletion

Ali K. Ahrabi[1,6], François Jouret[1], Etienne Marbaix[2], Christine Delporte[3], Shigeo Horie[4], Sharon Mulroy[5], Catherine Boulter[5], Richard Sandford[5] and Olivier Devuyst[1]

[1]Division of Nephrology, Université catholique de Louvain Medical School, Brussels, Belgium, [2]Division of Pathology, Université catholique de Louvain Medical School, Brussels, Belgium, [3]Laboratory of Biological Chemistry and Nutrition, Université Libre de Bruxelles Medical School, Brussels, Belgium, [4]Department of Urology, Teikyo University, Tokyo, Japan, [5]Department of Medical Genetics, Cambridge Institute of Medical Research, Hills Road, Cambridge, UK and [6]Renal Division, Department of Medicine, Brigham and Women's Hospital and Harvard Medical School, Boston, MA 02115, USA

Correspondence and offprint requests to: Olivier Devuyst; E-mail: Olivier.Devuyst@uclouvain.be

Abstract

Background. The homozygous deletion of *Pkd1* in the mouse results in embryonic lethality with renal cysts and hydrops fetalis, but there is no precise data on the segmental origin of cysts and potential changes associated with polyhydramnios.
Methods. We used *Pkd1*-null mice to investigate cystogenesis and analyze the amniotic fluid composition from embryonic day 12.5 (E12.5) to birth ($n = 257$ embryos).
Results. Polyhydramnios was consistently observed from E13.5 in $Pkd1^{-/-}$ embryos, in absence of placental abnormalities but with a significantly higher excretion of sodium and glucose from E13.5 through E16.5, and increased cyclic adenosine 3'5-monophosphate (cAMP) levels at E14.5 and E15.5. The $Pkd1^{-/-}$ embryos started to die at E13.5, with lethality peaking at E15.5, corresponding to the onset of cystogenesis. The first cysts in $Pkd1^{-/-}$ kidneys emerged at E15.5 in mesenchyme-derived segments at the cortico-medullary junction, with a majority of glomerular cysts and fewer proximal tubule cysts (positive for megalin). The cysts extended to ureteric bud-derived collecting ducts (positive for *Dolichos biflorus* agglutinin lectin) from E16.5.
Conclusions. These studies indicate that *Pkd1* deletion is associated with a massive loss of solutes (from E13.5) and increased cAMP levels (E14.5) associated with polyhydramnios. These abnormalities precede renal cysts (E15.5), first derived from glomeruli and proximal tubules and later from the collecting ducts, reflecting the expression pattern of *Pkd1* in maturing epithelial cells.

Keywords: cystogenesis; glomerular and proximal tubule cysts; low-molecular-weight protein; megalin; polyhydramnios

Introduction

Autosomal dominant polycystic kidney disease (ADPKD) is one of the most prevalent monogenic disorders, leading to end-stage renal disease in approximately half of the affected patients [1]. ADPKD is caused by mutations of either *PKD1* or *PKD2*, the genes that encode polycystin-1 and polycystin-2, respectively. These two proteins, which are located in the primary cilium, interact *in vivo* to regulate the proliferation and differentiation of renal tubular cells via various signalling pathways [2]. *PKD1* and *PKD2* are widely expressed throughout different foetal and adult tissues, explaining why ADPKD can affect extrarenal tissues including the liver, the pancreas and the arteries. In ADPKD kidneys, cysts originate from a small number of nephrons and possess functional and molecular characteristics of various nephron segments [3].

During normal human nephrogenesis, *PKD1* mRNA is absent from the uninduced mesenchyma and the emerging ureteric bud. From 10 weeks, a strong *PKD1* signal appears in the first set of differentiated proximal tubules (PT) from their glomerular origin. From 10 to 24 weeks, the differentiated PT express high levels of *PKD1* mRNA. At week 15, a discrete *PKD1* expression is also detected in the distal nephron and ureteric bud branches, persisting at a moderate level during foetal life [4]. In mouse embryonic kidneys, *Pkd1* is not expressed in the ureteric bud and comma and S-shaped bodies, and weakly expressed in induced metanephric mesenchyme from embryonic Day 13.5 (E13.5), to increase intensely in differentiating PT from E15.5 [5]. Several mouse models carrying mutations in *Pkd1* have been reported. All *Pkd1* knockout (KO) embryos die *in utero* by developing massive polycystic kidney disease, hydrops fetalis and polyhydramnios [5–10]. Some models are also characterized by vascular fragility [7] and cardiovascular and skeletal development defects [5], suggesting that the type of mutation in *Pkd1* may influence

the severity of the phenotype and the stage of lethality. Taken together, these studies showed that polycystin-1 does not play a major role in early nephrogenesis, as the latter is normal in *Pkd1* mutant embryos [5–7]. Instead, polycystin-1 may participate in epithelial cell differentiation and tubular extension in late nephrogenesis.

While previous studies pointed to the severe renal cystogenesis and extrarenal phenotype of *Pkd1* embryos, there has been no detailed investigation of the time-course and segmental origin of the cysts. Early functional abnormalities in human ADPKD include impaired urinary concentrating capacity [1,2] and urinary excretion of PT markers [11]. However, the factors contributing to polyhydramnios in *Pkd1* KO mice, including potential abnormalities in the placenta [12], remain unknown. In this study, we used a mouse model with a targeted deletion of *Pkd1*, resulting in a *Pkd1*-null allele [9], to investigate daily survival and cystogenesis *in utero*, as well as placental morphology and amniotic fluid (AF) volume and composition. Our data show that the loss of *Pkd1* is associated with a massive loss of solutes from E13.5 along with increased cyclic adenosine 3'5-monophosphate (cAMP) levels in the AF. These functional abnormalities precede the renal cysts, which are first detected in mesenchyme-derived glomerulus and PT segments and later in the collecting ducts.

Materials and methods

Pkd1 mice and in utero analyses

Studies were conducted on a *Pkd1* mouse model that was obtained by targeting the exons 2 to 5 and part of the exon 6 of *Pkd1*, resulting in a null allele [9,13]. The original stock of mice (mixed 129/sv/C57BL/6J background) was later backcrossed (at least six generations) to the C57BL/6J background. Heterozygous *Pkd1* mice, aged 10–15 weeks, were crossed to generate homozygous $Pkd1^{-/-}$ embryos. The gestational age was dated by appearance of the vaginal plug on the morning after mating, and designated as Day 0.5 (E0.5). Pregnant mice were sacrificed by cervical dislocation, and a caesarean section was performed to remove the uterus intact. The uterus was dissected and the embryos were removed under sterile, RNase-free conditions. The survival rate was based on embryos displaying a body movement or heart beating under microscopic examination. The embryos were placed on ice-cold Petri dishes and dissected to aspirate the AF and to harvest the kidneys. The studies covered the embryonic days E12.5 to E18.5 among a total of 257 embryos. We also used $Pkd1^{del17-21\beta geo}$ mouse embryos to investigate the expression of *Pkd1* in early tubulogenesis [5]. All protocols complied with the National Research Council Guide for the Care and Use of Laboratory Animals and were approved by the local ethics committee.

Antibodies and markers

Sheep polyclonal antibodies against megalin (a gift of Dr. P. Verroust, INSERM, Paris, France) and uromodulin (Biodesign Int., Saco, ME); goat polyclonal antibodies against PECAM-1 (CD31, Santa Cruz Biotechnology, Santa Cruz, USA); rabbit polyclonal antibodies against aquaporin-1 (AQP1) (Chemicon-Millipore, Billerica, MA), aquaporin-2 (AQP2) (Sigma, Saint Louis, MO) and podocin (P35, a gift of Dr. C. Antignac, INSERM); mouse monoclonal antibodies against polycystin-1 (7E12, Santa Cruz Biotechnology); and *Dolichos biflorus* agglutinin (DBA) lectin (Sigma) were used.

The rabbit polyclonal antibody, anti-leucine-rich repeats (LRR), was raised against the N-terminal LRR domain of polycystin-1. Rabbits were immunized with purified His-tagged LRR domain (amino acids 27–360) expressed as a bacterial fusion protein; and antibodies purified using protein-A agarose as previously described [14]. The specificity of the

purified anti-LRR antibodies was confirmed by ELISA (not shown) and Western blot analysis against both the polycystin-1 N-terminal fusion protein and the recombinant polycystin-1 LRR (Suppl. Fig. 1). Previous studies have shown that the anti-LRR antibodies were able to immunoprecipitate the *in vitro* translated N-terminal half of polycystin-1, and that immunostaining was abolished with preadsorption of antibody with fusion protein [14].

Immunohistochemistry

Embryonic kidney samples were fixed in 4% paraformaldehyde (Boehringer Ingelheim, Heidelberg, Germany) in 0.1 mol/L phosphate buffer, pH 7.4, prior to embedding in paraffin as described [13]. Six-micrometre sections were cut and stained with hematoxylin and eosin. Additional sections were incubated for 30 min with 0.3% hydrogen peroxide to block endogenous peroxidase. Following incubation with 10% normal serum for 20 min, sections were incubated for 45 min with the primary antibodies diluted in PBS containing 2% bovine serum albumin (BSA). After washing, sections were successively incubated with biotinylated secondary anti-immunoglobulin (Ig) G antibodies, avidin–biotin peroxidase and aminoethylcarbazole (Vectastain Elite, Vector Laboratories). The M.O.M. kit (Vector Laboratories) was used for mouse-derived antibodies. Sections were viewed under a Leica DMR coupled to a Leica DC300 digital camera (Leica, Heerbrugg, Switzerland). Kidney sections of both $Pkd1^{-/-}$ and $Pkd1^{+/+}$ embryos ranging from E13.5 to E18.5 ($n = 4$ per embryonic day) were examined.

Staining for β-galactosidase activity in $Pkd1^{del17-21\beta geo}$ kidneys

Staining for β-galactosidase activity in frozen tissue sections was carried out as previously described [5]. Tissues were fixed in X-gal fixative (0.2% paraformaldehyde (PFA), 0.1 M PIPES buffer, 2 mM MgCl₂, 0.1 M EGTA, pH 7.3) at 4°C and cryoprotected in 30% sucrose/2 mM MgCl₂ before being snap frozen on LN₂ and stored at −160°C in LN₂ until sectioned. Fifteen-micrometre tissue sections were fixed at 4°C for 10 min in X-gal fixative and rinsed briefly in ice-cold PBS/2 mM MgCl₂. The sections were permeabilized by washing in detergent rinse (0.1 M phosphate buffer, pH 7.3, 2 mM MgCl₂, 0.01% sodium deoxycholate, 0.02% NP-40) at 4°C for 30 min, and stained in X-Gal staining solution (1mg/ml X-gal, 0.1 M phosphate buffer pH 7.3, 2 mM MgCl₂, 0.01% sodium deoxycholate, 0.02% NP-40, 5 mM potassium ferricyanide and 5 mM potassium ferrocyanide) at 37°C overnight in the dark. Stained sections were washed twice in PBS/2 mM MgCl₂, rinsed in H₂O and counterstained for 2 min with nuclear fast red (Vector Laboratories). The sections were rinsed in water for 10 min, dehydrated with 5-min exchanges through graded methanol (50%, 70%, 90% and 100%) and cleared in Histoclear (Fischer Chemicals). Sections were mounted using Vectamount (Vector Laboratories).

Morphometric analyses of the placenta

Volumic density of four different compartments of the placenta (the chorionic plate with stem villi, the labyrinth, the spongiotrophoblast and the giant cells) was determined by point counting, using a GF Planachromat 12.5× objective on a Jenamed 2 microscope (Jena, Jena, Germany) equipped with GF-PW 10× oculars containing a 100 crosses grid. A random whole histological cross-section was analysed for six placentas from $Pkd1^{+/+}$ and $Pkd1^{-/-}$ embryos at E13.5 by a pathologist unaware of the mouse genotype.

Analyses of AF

The AF samples were prospectively collected from live embryos of pregnant $Pkd1^{+/-}$ females from E12.5 to E18.5. Each embryo was placed inside a pre-weighed chamber before inserting a BD Micro-Fine Insulin needle, 29G × 12.7 mm, into the amniotic sac for AF aspiration. After careful aspiration, the foetal membrane was ruptured and opened up completely in order to collect all the remaining fluid. The total volume of the AF was measured in pre-weighed sterile tubes (intra-assay error <5%). Aliquots of AF were obtained at the time of aspiration and stored at −20°C. The concentrations of sodium and glucose were measured with Synchron CX5 PRO analyser (Beckman Coulter, Fullerton, CA). The concentrations of the low-molecular-weight (LMW) protein CC16 (Clara cell protein 16 kD) was determined using a sensitive radioimmunoassay as described [15].

Table 1. Survival rate of *Pkd1*-mutant embryos

Crossed mice n	Embryonic Age	$Pkd1^{-/-}$ n: A (D)	$Pkd1^{+/+}$ n: A (D)	$Pkd1^{+/-}$ n: A (D)	Total embryos n
2	E12.5	3 (0)	3 (0)	12 (0)	18
5	E13.5	9 (1)	6 (0)	12 (0)	28
6	E14.5	12 (0)	9 (0)	17 (0)	38
7	E15.5	10 (4)	11 (0)	19 (0)	44
5	E16.5	5 (8)	10 (0)	16 (0)	39
5	E17.5	3 (8)	8 (0)	13 (0)	32
5	E18.5	3 (9)	9 (0)	15 (0)	36
4	At birth	0 (4)	6 (0)	13 (0)	23

A, alive; D, dead; n, number.

cAMP measurement

For cAMP measurement, AF (30 µl) was mixed with 300 µl of absolute ethanol, vortexed and centrifuged at 3500 g for 20 min at 4°C. The supernatant was collected and lyophilized using a Speed-Vac concentrator. cAMP levels were determined using a cAMP [^{125}I] Biotrak Assay (Amersham, Buckinghamshire, UK) following the acetylation procedure described in the assay. The lyophilized AF samples and cAMP standards (ranging from 2 to 128 fmol/100 µl) were submitted to acetylation by the addition of a mixture of acetic anhydride triethylamine (1:2; v:v). A duplicate of 100 µl aliquots from all standards and samples was pipetted into polypropylene tubes, then 100 µl of antiserum (except in tubes for the determination of non-specific), and 100 µl of cAMP [^{125}I] were added into all tubes, prior to being vortexed, and finally incubated for 4 h at 4°C. After the incubation, 500 µl of Amerelex-M secondary antibody reagent was added to each tube. The tubes were vortexed and then incubated for 10 min at room temperature. The antibody-bound fraction was separated by centrifugation at 2500 g for 15 min, and the supernatant liquid was discarded by careful aspiration. The radioactivity was counted in duplicate for 2 min in a gamma counter.

Data analysis

Comparisons between groups were performed using two-tailed unpaired Student's *t*-test (GraphPad, San Diego, CA). Significance level was $P < 0.05$.

Results

Survival rate and polyhydramnios in $Pkd1^{-/-}$ embryos

Embryonic lethality was observed in $Pkd1^{-/-}$ embryos as early as E13.5, with a survival rate that sharply declined at E15.5. Only 25% (3/12) of $Pkd1^{-/-}$ embryos survived at E18.5, and none at birth. By contrast, all wild-type and heterozygous *Pkd1* embryos survived to birth (Table 1). The first abnormality found in $Pkd1^{-/-}$ embryos was the polyhydramnios, consistently observed from E13.5 (Figure 1A–C). The time-course analysis revealed a progressive and continuous increase in the total AF volume in $Pkd1^{-/-}$ mice, contrasting with the stability observed between E12.5 and E17.5 in both wild-type and heterozygous mice. The AF volume was significantly higher at all time points from E13.5 to E18.5 in $Pkd1^{-/-}$ vs. both $Pkd1^{+/+}$ and $Pkd1^{+/-}$ embryos (Figure 1D).
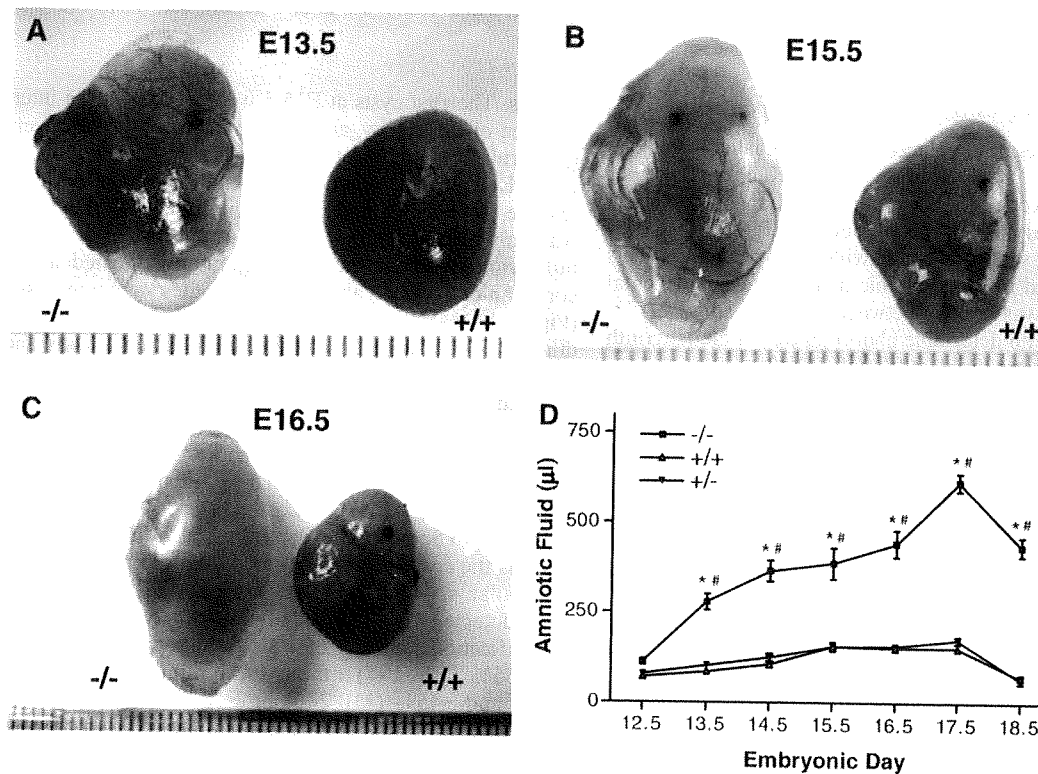

Fig. 1. Polyhydramnios in $Pkd1^{-/-}$ embryos. (A–C) $Pkd1^{-/-}$ embryos with massive polyhydramnios shown here inside the mother's uterine membrane at different stages of development in comparison with $Pkd1^{+/+}$ wild-type embryos: (A) E13.5, (B) E15.5 (C) E16.5. Bar = millimetre scale. (D) Time-course of amniotic fluid volume at each time point according to the *Pkd1* genotype (*n* = 6 to 19 embryos at each time point). The total amniotic fluid volume values were significantly higher in $Pkd1^{-/-}$ vs. $Pkd1^{+/+}$ and $Pkd1^{+/-}$ from E13.5 to E18.5. *$P < 0.0001$; #$P < 0.0001$, $Pkd1^{-/-}$ vs. $Pkd1^{+/-}$.
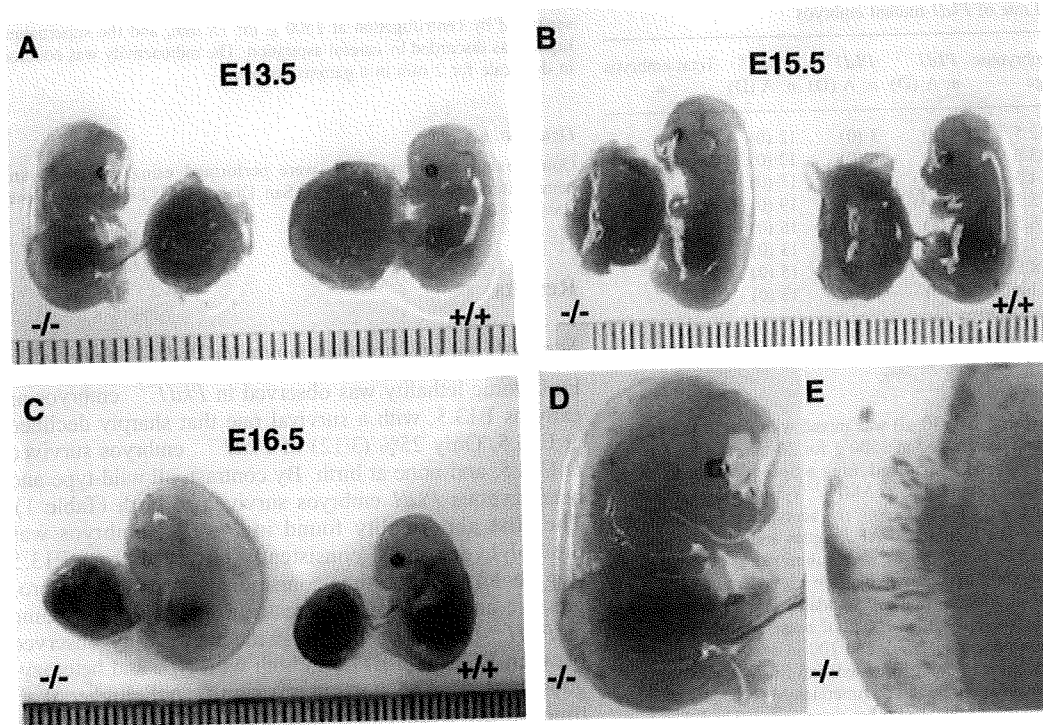
Fig. 2. Hydrops fetalis and vascular fragility in $Pkd1^{-/-}$ embryos. (A–C) $Pkd1^{-/-}$ embryos showed hydrops fetalis (generalized oedema, most visible on the back of the body) at E13.5 (A), E15.5 (B) and E16.5 (C). **D.** Focal haemorrhage in a $Pkd1^{-/-}$ embryo aged E13.5, demonstrating vascular fragility. **E.** High magnification of a $Pkd1^{-/-}$ embryo's back at E16.5, showing subcutaneous oedema and vascular fragility. Bar = millimetre scale.

Histological analysis of the Pkd1-mutant placentas

As abnormalities of the placental labyrinth layer have been described in a $Pkd1^{-/-}$ mouse model (K. Piontek *et al.*, unpublished work [12]), we performed a detailed morphometry analysis of the placentas of $Pkd1$ mice at E13.5, the first stage associated with polyhydramnios. This analysis showed that the volumic density of each placental compartment was similar between $Pkd1^{+/+}$ and $Pkd1^{+/-}$ embryos, with no detectable abnormalities in the labyrinth and the spongiotrophoblast (Suppl. Fig. 2).

Hydrops fetalis and vascular fragility in Pkd1^{-/-} embryos

In addition to polyhydramnios, $Pkd1^{-/-}$ embryos showed a typical phenotype of hydrops fetalis resulting in tissue edema, detectable from E13.5 and throughout gestation (Figure 2A–C). Edema of the back of the body caused a vertical shape, preventing $Pkd1^{-/-}$ embryos from being curved as the wild-type embryos. Moreover, the $Pkd1^{-/-}$ embryos showed areas of focal haemorrhage in different regions of the body, such as the neck and abdomen (Figure 2D, E). The vascular rupture could be observed as early as E13.5 and continuing to E18.5.

Pattern of cystogenesis in the Pkd1^{-/-} embryonic kidneys

Histological analysis (Figure 3) showed that the renal cysts in $Pkd1^{-/-}$ embryos were first detected at E15.5 (Figure 3B), consistent with the other $Pkd1$-mutant mouse models. The first cysts at E15.5 were located in the internal area of the kidney, and a large majority of them were glomerular cysts characterized by the cystic enlargement of the Bowman space and the presence of glomerular tufts (Figure 3F and Figure 4). The glomerulocystic phenotype was only observed for glomeruli located in the deep medulla zone, whereas superficial glomeruli located in the cortex among comma and S-shaped bodies were non-cystic (Figure 4A). At high magnification, the cysts arise from the dilation of the Bowman capsule, with flattened cells and discontinuous cell lineage. The podocytes, typically organized in a crown surrounding the capillaries in the young glomeruli, showed no abnormalities (Figure 4B). Immunostaining for the endothelial marker CD31/PECAM-1 identified the normal glomerular vascularization in these sections (Figure 4C, D).

From E16.5, cystogenesis progressed from the medulla towards the cortical area, still involving glomeruli as well as tubular segments (Figure 3G). By E18.5 the cysts were detected in all areas of the kidney (Figure 3H). Quantification revealed that glomerular cysts accounted for ~65% (128/197) of the total number of cysts at E15.5 and ~45% (110/246) at E16.5 (Table 2). Apart from atrophic lesions of the glomerular tuft, which were observed from E16.5, there was no evidence for fibrosis, inflammatory infiltrate, tubular casts or epithelial hyperplasia in the $Pkd1^{-/-}$ kidneys. Of note, even in mutant embryos, nephrogenesis continued on until birth in the external cortex.
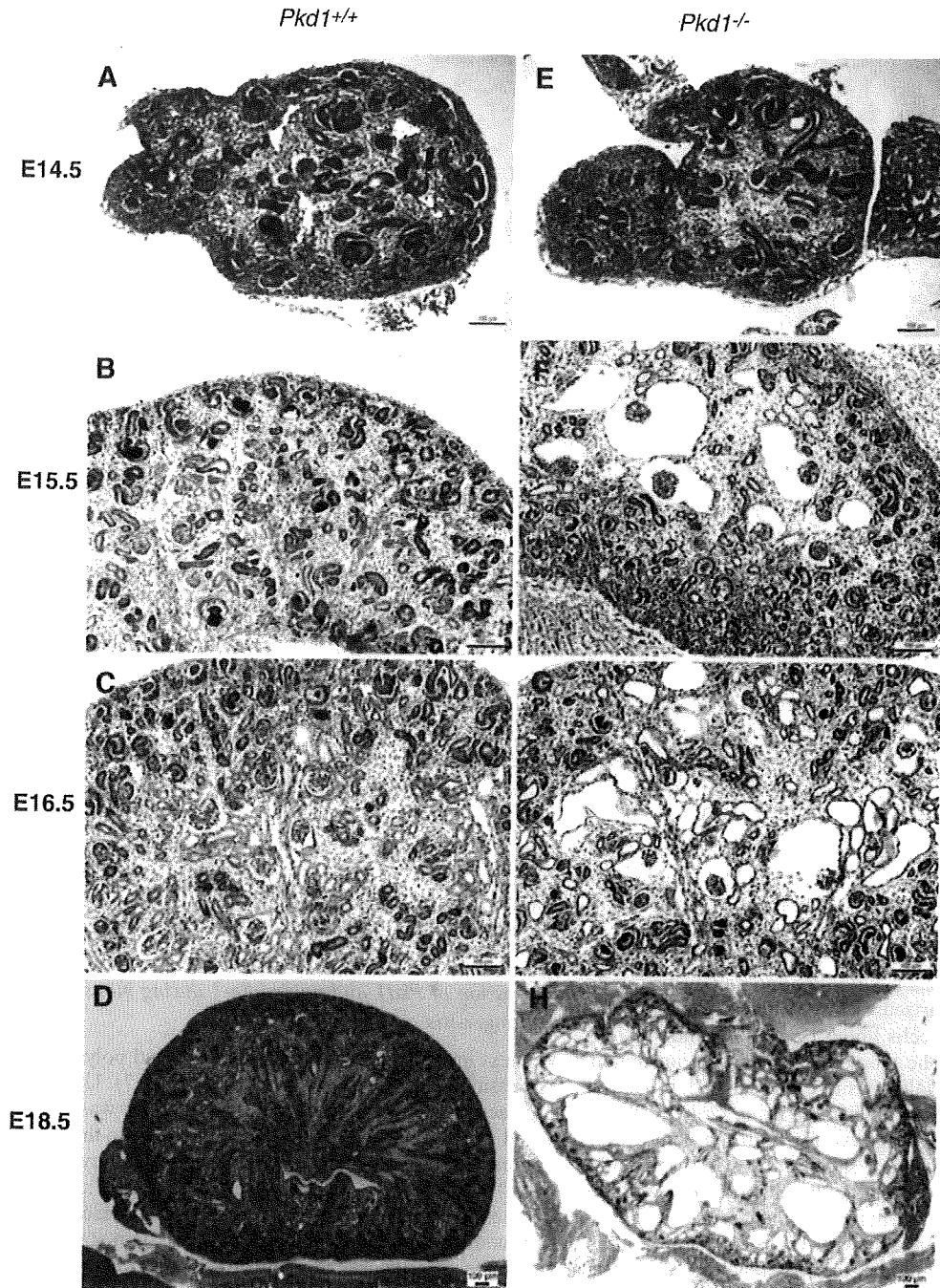
Pkd1+/+   Pkd1-/-

Fig. 3. Stages of renal development in *Pkd1* embryos. Representative sections (hematoxylin and eosin staining) of *Pkd1*$^{+/+}$ (A–D) and *Pkd1*$^{-/-}$ (E–H) embryonic kidneys at different stages of development. Progressive cyst formation, starting from glomeruli and later extending to tubular segments, is observed in *Pkd1*$^{-/-}$ kidneys beginning at E15.5 (F–H). Bar = 100 µm.

Segmental origin of the cysts in Pkd1-mutant kidneys

To further characterize the segmental origin of the cysts, serial sections of *Pkd1*$^{-/-}$ kidneys were stained with megalin, a multi-ligand receptor that is specifically expressed in PT cells [16], and DBA lectin, a marker of the distal convoluted tubule and the collecting duct [17] (Figure 5). No

cyst was observed at E14.5, whereas developing tubular profiles positive for megalin or DBA lectin were detected (Figure 5A, E). At E15.5, some of the cysts at the corticomedullary junction were stained with megalin, whereas no cysts were stained with DBA lectin (Figure 5B, F). At E16.5, a fraction of cysts located in medulla and corticomedullary area were positive for megalin (70/246, 28%),
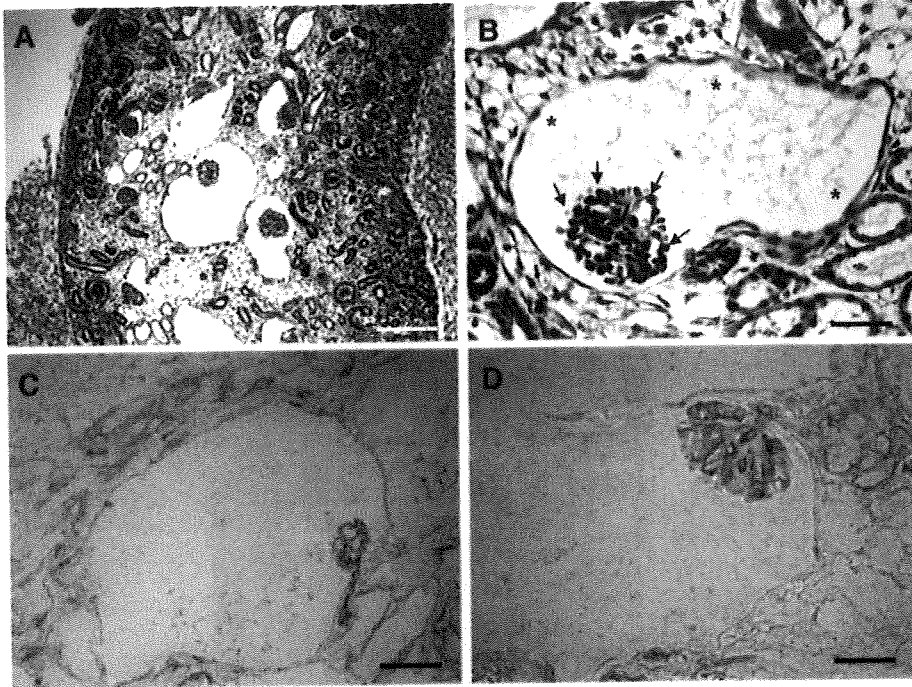
Fig. 4. Glomerular cysts in *Pkd1*-null embryos. (**A, B**) At E15.5, a typical picture of glomerulocystic kidney disease was observed in *Pkd1*$^{-/-}$ embryos. The glomerulocystic phenotype was only observed for glomeruli located in the deep medulla zone, whereas superficial glomeruli located in the cortex among comma and S-shaped bodies were non-cystic (**A**). At high magnification (**B**), the cysts arise from the dilation of the Bowman capsule, with flattened cells and discontinuous cell lineage (asterisk). The podocytes, typically organized in a crown surrounding the capillaries in the young glomeruli (arrows), showed no abnormalities. The start of early proximal tubules could be seen in some glomerular cysts, without tubular dilation at E15.5. Immunostaining for CD31 (**C–D**) was used as a marker of glomerular vascularization in cysts identified at E18.5. Bar = 80 μm (A); 20 μm (B, D); 40 μm (C).

or less frequently, DBA lectin (42/246, 17%) (Figure 5C, G; Table 2). There was no cross-reactivity between megalin and DAB lectin in the same cyst (Figure 5B–H).

Further analyses showed that the staining for megalin, which was strictly apical in wild-type and non-cystic tubule profiles, was less polarized, diffusely increased or even absent in the epithelial cells lining PT cysts in the *Pkd1*$^{-/-}$ kidneys (Figure 6). The glomerular cysts were unstained, except for some megalin-positive PT cells identified at the urinary pole of the Bowman capsule. Only ~10% of the tubular cysts were negative for both markers (Table 2). We could not obtain clear staining for AQP1 (PT marker), uromodulin (thick ascending limb marker) or AQP2 or calbindin (collecting duct markers) at any stage, even after antigen retrieval (data not shown). These data show that, in this *Pkd1*-null mouse model, the first renal cysts are de-

tected at E15.5 in mesenchyme-originated tissues rather than ureteric bud-originated tissues, and that a majority of glomerular cysts is observed at E15.5 and E16.5.

Expression of Pkd1 and polycystin-1 during mouse nephrogenesis

We next investigated the pattern of *Pkd1* and polycystin-1 expression in the developing mouse (Figure 7). Using the β-galactosidase reporter gene, *Pkd1* expression was not detected in the pronephros or mesonephros prior to the development of the definitive metanephric kidney in the *Pkd1*$^{del17-21\beta geo}$ $^{+/-}$ mouse. From E13.5–E15.5, weak *Pkd1* expression was seen in the condensed mesenchyme surrounding the ureteric bud tips and weakly in some cells within the uncondensed mesenchyme but not in the ureteric

Table 2. Segmental origin of the cysts in *Pkd1*-null embryonic kidneys

Age	Kidney sections (n)[a]	Glomerular cysts (n)	Megalin[b]	n	DBA lectin[b]	n	Undefined cysts (n)	Total cysts (n)
E13.5	8	0	++	0	+	0	0	0
E14.5	8	0	++	0	++	0	0	0
E15.5	10	128	++	54	++	0	15	197
E16.5	8	110	++	70	++	42	24	246

[a]These sections were obtained from four to five embryos.
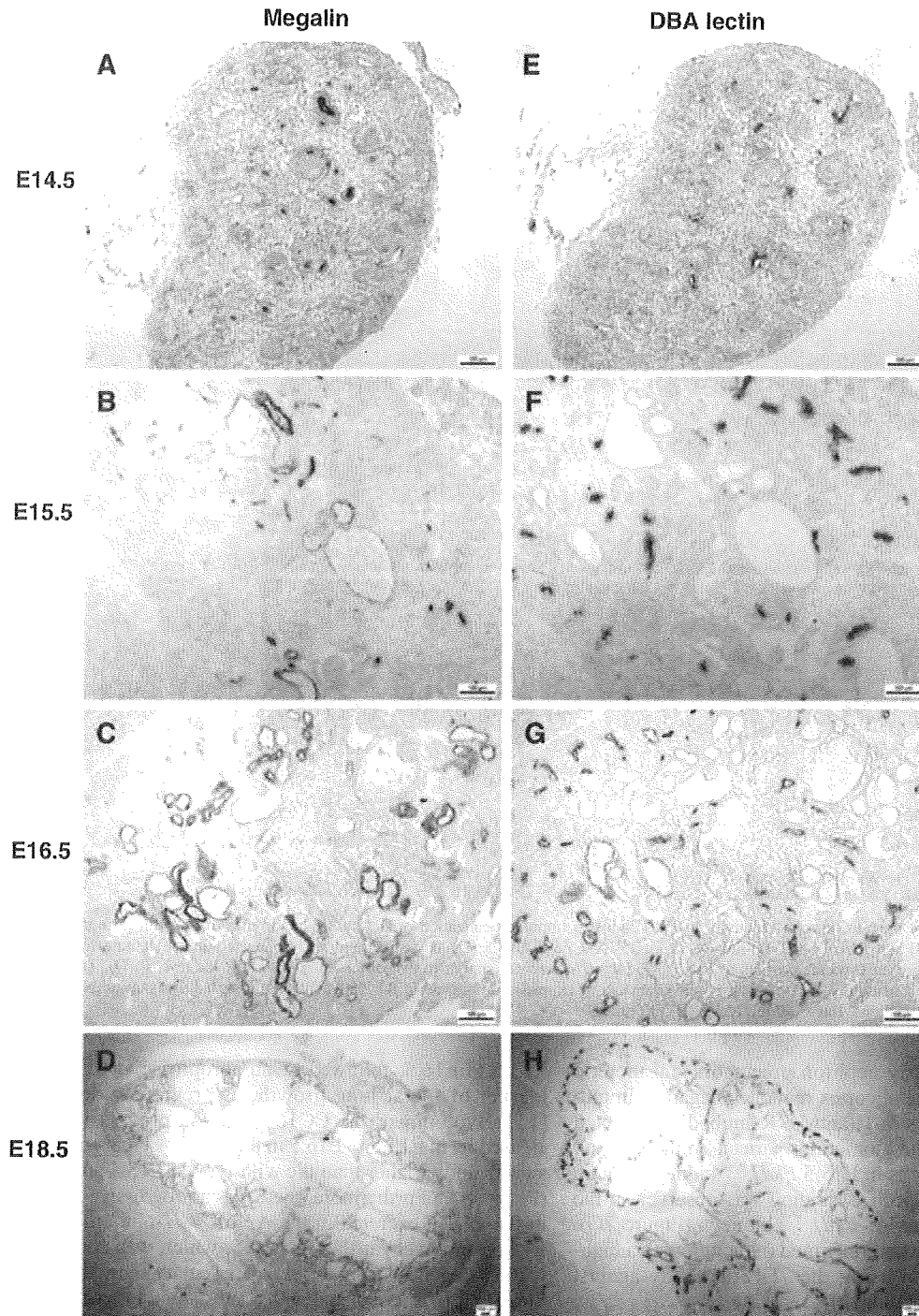[b]Staining intensity: +, weak positive staining; ++, strong positive staining.

Megalin   **DBA lectin**

Fig. 5. Segmental origin of cysts in *Pkd1*^{−/−} embryonic kidneys. Serial sections of *Pkd1*^{−/−} embryonic kidneys at different stages of development stained with megalin, a marker of the proximal tubule (A–D), and DBA lectin, a marker of the distal tubule and collecting duct (E–H). Non-cystic tubule profiles are stained at E14.5, without cross-reactivity between the two markers (A, E). At E15.5, some cysts are stained with megalin (B), whereas DBA staining is still restricted to non-cystic tubules (F). At E16.5 and E18.5, some cysts are stained with megalin, whereas other cysts are positive for DBA lectin, indicating proximal vs. collecting duct origin respectively (C–D vs. G–H). There was no cross-reactivity between megalin and DAB lectin in the same cyst. Bar = 100 μm.

bud tips themselves. *Pkd1* expression was also seen in endothelial cells migrating into the S-shaped body to form the glomerulus. From E15.5, there was marked upregulation of

Pkd1 expression within the developing metanephros and in the glomerular parietal epithelium, differentiating PT and collecting ducts (Figure 7A, B). Vascular staining was also
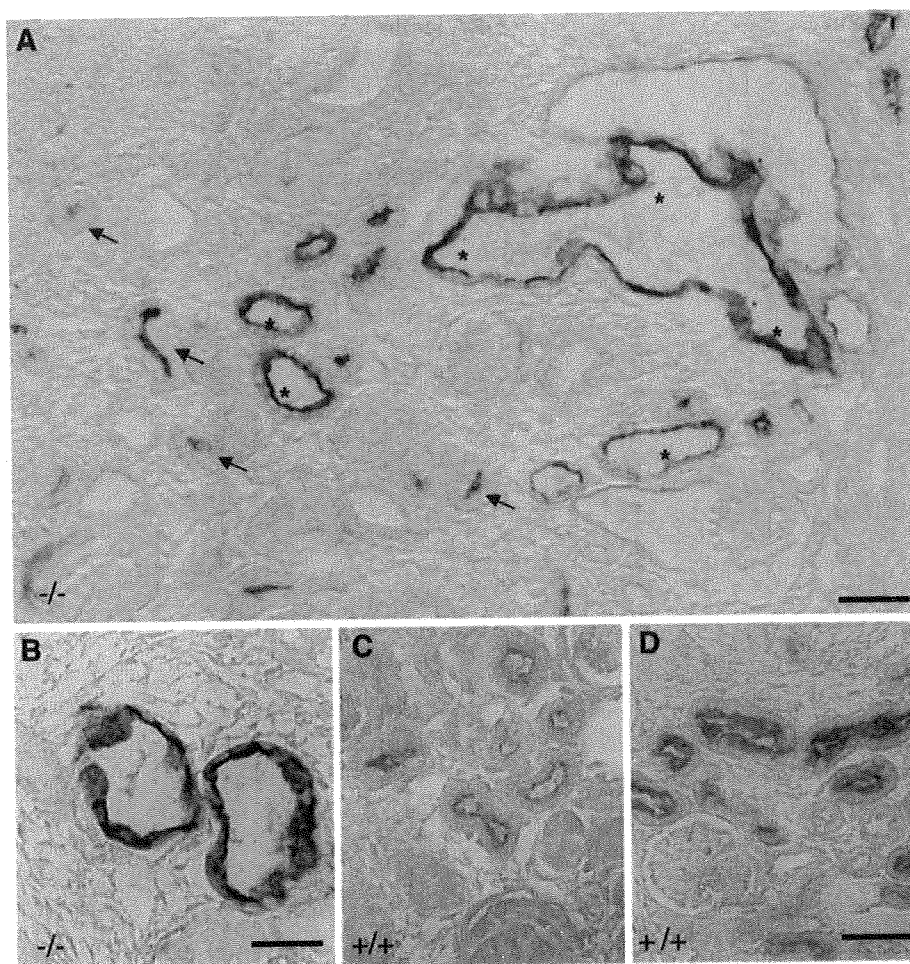
Fig. 6. Distinct patterns of megalin immunoreactivity in *Pkd1* kidneys. Immunolocalization of the multi-ligand receptor megalin in representative sections of *Pkd1*$^{-/-}$ (A, B) and *Pkd1*$^{+/+}$ (C, D) kidneys at E16.5 (A–C) and E18.5 (D). A distinct and well-delineated apical staining for megalin is observed in non-cystic proximal tubule profiles of *Pkd1*$^{-/-}$ kidneys (A, arrows), similar to that observed in wild-type kidneys (C, D). This pattern contrasts with the increased reactivity, loss of polarity and even loss of expression observed in the flattened cells lining adjacent cystic profiles (A, asterisks; B, higher magnification). Bar = 40 µm (A, C, D); 20 µm (B).

detected, whereas early nephron precursors and ureteric bud tips in the peripheral cortex remained negative. Immunostaining for polycystin-1 (anti-LRR antibodies) detected a specific signal in the glomerular parietal epithelium and in the PT epithelial cells in E15.5 *Pkd1*$^{+/+}$ kidneys (Figure 7E–F), whereas no specific staining was observed in the corresponding regions of *Pkd1*$^{-/-}$ kidneys (Figure 7G). This staining pattern was confirmed (although with a higher background) when using the 7E12 antibody against polycystin-1 (data not shown).

Massive loss of solutes and increased cAMP levels in AF

The AF collected from E13.5 to E16.5 was analyzed in order to calculate the amount of solute excreted in each genotype (Figure 8). The *Pkd1*$^{-/-}$ embryos were characterized by a significantly higher excretion of sodium and glucose from E13.5 through E16.5 (Figure 8A, B). Time-course analysis of the LMW protein CC16 in the AF of the wild-type embryos revealed a progressive decrease from

E13.5 to E16.5, followed by an abrupt rise at E17.5 as a marker of foetal lung growth, as previously described [15]. By contrast, the CC16 excretion progressively increased from E13.5 to E16.5 in the *Pkd1*$^{-/-}$ embryos, being significantly higher than the wild-type at E15.5 and E16.5 (Figure 8C). Furthermore, there was a progressive increase in the cAMP excreted in the AF of *Pkd1*-null embryos at E14.5, and even further at E15.5, which was concurrent with cystogenesis (Figure 8D). These data show that deletion of *Pkd1* is associated with a substantial loss of solutes, including the LMW protein CC16 before the onset of lung growth, and increased cAMP levels in the AF.

Discussion

In this study, we have analysed the consequences of *Pkd1* deletion on the time-course and pattern of cystogenesis, the structure of the placenta and the AF volume and composition in mouse embryos. The *Pkd1*-null embryos start to die
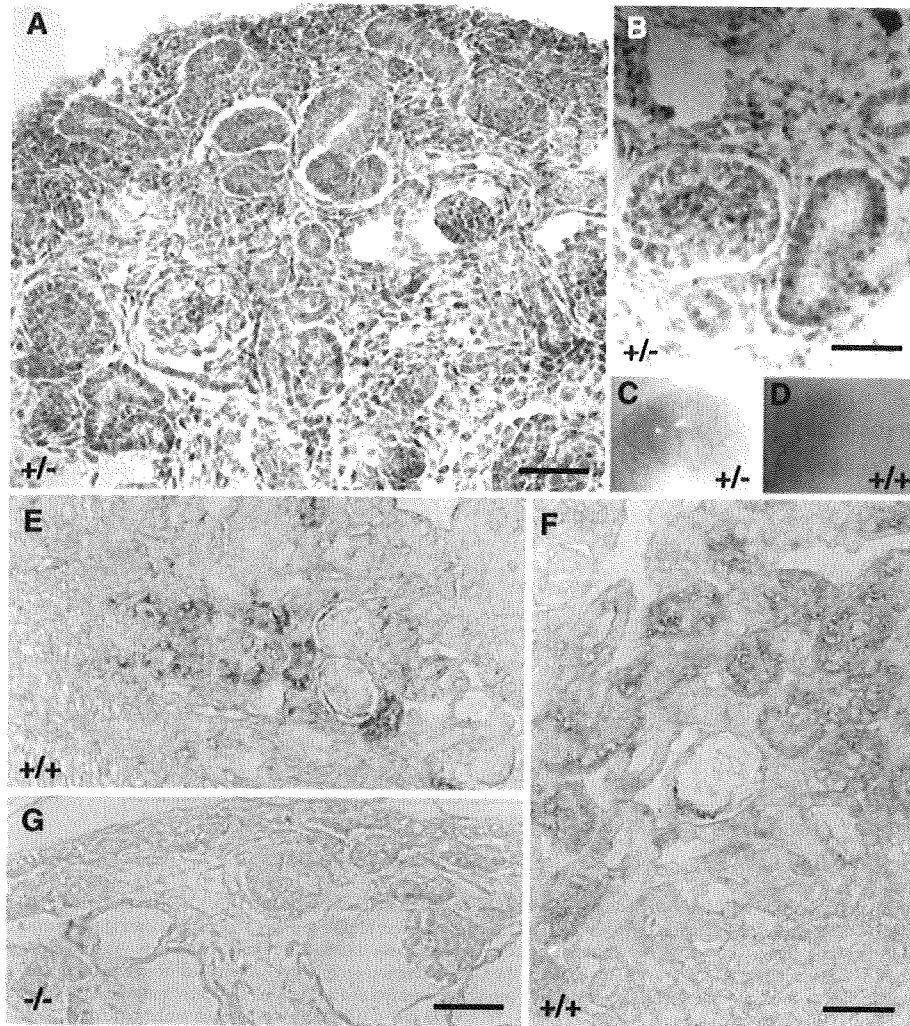
Fig. 7. Expression of *Pkd1* and polycystin-1 in the developing mouse kidney. (**A–D**) LacZ staining for *Pkd1* expression in $Pkd1^{del17-21\beta geo\ +/-}$ mice. The expression of *Pkd1* in the glomerular parietal epithelium and in proximal and more distal tubule epithelial cells is seen at low magnification (panel A, E16.5). Note that the renal capsule is also a site of *Pkd1* expression. The glomerular and proximal tubular expression is detected as early as E15.5 (panel B). Panels C (+/−) and D (+/+) are positive and negative whole mount controls for the lacZ staining, respectively. (**E–G**) Immunostaining for polycystin-1 (anti-LRR antibodies) in E15.5 *Pkd1* kidneys. A clear signal is observed in the glomerular parietal epithelium and in the proximal tubule epithelial cells of $Pkd1^{+/+}$ kidneys (panels E and F). No specific staining is observed in the corresponding region of a *Pkd1* KO kidney (panel G). Bar = 30 μm (A, F); 20 μm (B); 40 μm (E, G).

at E13.5, with consistent features including hydrops fetalis, renal cysts and vascular fragility, in absence of placental abnormalities. This *Pkd1*-null model is characterized by an early polyhydramnios, with an excessive loss of various solutes, including cAMP, in the AF. These features precede the development of renal cysts, which are first detected in glomeruli and PT, and later in distal nephron segments.

Nephrogenesis in mouse and man is characterized by a repetitive and reciprocal induction between the ureteric bud and the metanephric mesenchyme, resulting in the formation of mature kidneys before birth. The first cysts in $Pkd1^{-/-}$ embryonic kidneys are observed at E15.5, starting in mesenchyme-originated tissues, with the majority of cysts arising from mature glomeruli and a significant proportion from the PT segments as indicated by positive

megalin staining. These events are reflected by a rise in embryonic lethality at E15.5. The segmental cystogenesis in our model is consistent with the pattern of *Pkd1* expression in the mouse as reported by Boulter *et al.* [5] and further detailed here using lacZ staining on developing kidneys from $Pkd1^{del17-21\beta geo\ +/-}$ mice (Figure 7). In agreement with *in situ* hybridization data [18], these studies show that *Pkd1* expression is limited during early nephrogenesis, with weak expression in the mesenchyme and no expression in the ureteric bud. From E15.5, *Pkd1* expression increased dramatically in induced mesenchymal cells, including maturing PT, and subsequently, more distal nephron segments [5]. The initial and intense expression of *Pkd1* in glomerular parietal epithelium and PT is in line with the first cystic lesions observed here and in the
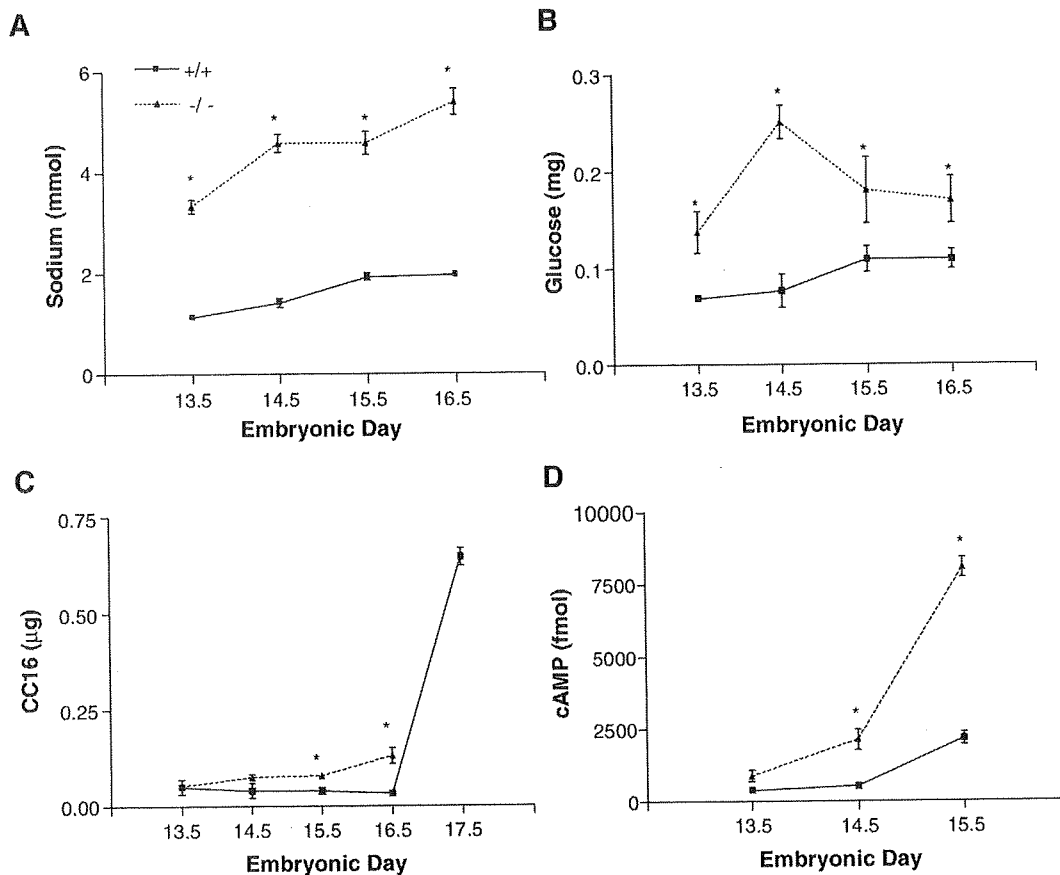
Fig. 8. Time-course of solute excretion in the amniotic fluid of *Pkd1* embryos. Total excretion of sodium (A), glucose (B), CC16 (C) and cAMP (D) in the amniotic fluid of *Pkd1*$^{+/+}$ vs. *Pkd1*$^{-/-}$ embryos. The excretion of sodium (A) and glucose (B) was higher in *Pkd1*$^{-/-}$ embryos during the course of embryogenesis (*$P < 0.0001$, $n = 4$ to 15 at each embryonic day). The excretion of CC16 progressively decreased from E13.5 to E16.5 in the wild-type embryos, followed by an abrupt rise at E17.5 due to foetal lung growth. By contrast, the CC16 excretion progressively increased from E13.5 to E16.5 in *Pkd1*$^{-/-}$ embryos, being significantly higher than the wild-type at E15.5 and E16.5 (no viable embryo at E17.5) (C). The excretion of cAMP (D) was significantly higher in *Pkd1*$^{-/-}$ vs. *Pkd1*$^{+/+}$ embryos at E14.5 and further at E15.5 (*$P < 0.02$, #$P < 0.0001$, $n = 4$ at each embryonic day).

Pkd1$^{del34/del34}$ mice [6]. Glomerular cysts have also been reported in the *Pkd1*$^{L/L}$ mouse model characterized by a severe phenotype including vascular defect leading to haemorrhagic lesions and lethality by E15.5 [7]. Furthermore, glomerular cysts were detected in the adult kidneys from two models of transgenic mice overexpressing normal *PKD1* [19] or *Pkd1* [20], suggesting the importance of a precise regulation of polycystin-1 expression for normal glomerular maturation and tubulogenesis.

Hydrops fetalis, a term used to describe foetuses with generalized oedema and cavity effusions, is observed in the *Pkd1*$^{-/-}$ embryos like in the majority of *Pkd1* KO mice thus far [5,7–9]. Fluid balance in the foetus integrates placental fluid transfer, capillary filtration, swallowing, lung secretion and urine production [21]. Accordingly, many features observed in the *Pkd1* mice may explain an interstitial fluid accumulation, including abnormal vascular permeability, cardiac malformations and impaired renal function. The *Pkd1*$^{-/-}$ embryos investigated here show a significant polyhydramnios, consistently observed from E13.5 and throughout development. By contrast, the AF

volume is stable across gestation in both wild-type and heterozygous *Pkd1* mice, followed by a sharp decrease at E18.5, similar to the human and mouse situation [21,22]. In addition to our model, polyhydramnios has only been reported in another *Pkd1*-null mouse [8]. Polyhydramnios may result from salt-losing tubulopathies or increased foetal urine output secondary to diabetes insipidus [23]. The AF fluid analyses demonstrated a massive loss of sodium and glucose in the *Pkd1*$^{-/-}$ embryos starting at E13.5, i.e. 2 days before cystogenesis. There is also an increased excretion of the LMW protein CC16 at E15.5 and E16.5 in the AF of *Pkd1*-mutant embryos, before the sharp increase due to lung maturation [15]. CC16 is typically reabsorbed by PT cells through the multi-ligand megalin receptor pathway [16]. We showed previously that the polarized expression of essential components of the PT endocytic apparatus (e.g. ClC-5 and vacuolar H^{+}-ATPase subunits) is acquired at E15.5 [24]. The co-expression of these molecules—including megalin as reported here—immediately after the onset of glomerular filtration [25] suggests an early maturation of PT function. Together with the abnormal megalin

expression observed in PT-derived cysts, the increased excretion of CC16 in the AF suggests that PT maturation may be altered in the *Pkd1*$^{-/-}$ mice. In that respect, it is interesting to note that an abnormal excretion of PT markers is an earliest functional defect in patients with ADPKD [11].

Placental malformations may also cause abnormal fluid balance in embryos. It has been suggested that abnormalities of the placental labyrinth layer, detected from E11.5, may cause *Pkd1*$^{-/-}$ foetal death [12]. By contrast, our morphometry analysis did not detect abnormalities in the four placental compartments, including the labyrinth layer (Suppl. Fig. 2). Thus, gross placental abnormalities cannot explain the hydrops fetalis and polyhydramnios observed at E13.5 in our model. As the phenotype of *Pkd1* mice is notoriously dependent on the genetic background, one could speculate that differences in placenta morphology could reflect the different background (129Sv vs. C57BL/6J, respectively) of the models.

We observed increased cAMP levels in the AF of *Pkd1*$^{-/-}$ embryos at E14.5 and E15.5, concomitant to cystogenesis. A progressive increase in cAMP in the AF has been reported in normal human pregnancy [26], which could reflect the progressive increase in glomerular filtration and the maturation of PT and response to parathyroid hormone [27]. As glomerular filtration—and tubular maturation (see above)—start at E14.5 in mouse, the increased levels observed at both E14.5 and E15.5 in *Pkd1*-null embryos could reflect epithelial tubular production, in addition to the maternal origin or production by the amniotic membranes. Previous studies have shown that increased levels of cAMP could play a major role in cyst formation, through stimulation of fluid secretion and cell proliferation (reviewed in [2]). In two cystic models orthologous to human autosomal recessive PKD (PCK rat) and nephronophthisis (*pcy* mouse), and one cystic model orthologous to human ADPKD (*Pkd2*$^{-/tm1Som}$ mouse), increased renal cAMP levels, paralleled with higher expression of AQP2 and arginine vasopressin (AVP) V2 receptor (V2R), have been reported [28–30]. Recently, Magenheimer *et al.* showed that embryonic kidney tubules from E13.5 to E15.5 could be stimulated by cAMP to form cyst-like structures of both proximal tubule and collecting duct origin, a process that is significantly enhanced in *Pkd1*$^{-/-}$ embryonic kidneys [31]. The mechanism responsible for increased cAMP production is probably multifactorial, involving the interaction of circulating AVP with the V2R in the collecting duct, together with decreased intracellular calcium levels which can activate adenylyl cyclase 6 and/or inhibits phosphodiesterase 1 [2]. The involvement of the V2R pathway has been substantiated by the effects of V2R antagonists in various genetic models of PKD, with decreased renal cAMP levels associated with slowed cyst and renal enlargement and improved renal function, motivating a multicentric trial to test the efficacy of a selective V2R antagonist in ADPKD patients [32].

The effects of V2R antagonists on cAMP generation and the cystic phenotype in ADPKD are based on the assumption that ADPKD cysts are predominantly of collecting duct origin. However, the deletion of *Pkd1* in this mouse model is associated with predominant glomerular

cysts at E15.5, followed by the development of (megalin-positive) PT cysts and later by collecting duct cysts. Accordingly, the V2R/AQP2 pathway, which is restricted to the collecting duct and not expressed in the glomerular parietal epithelium or in the PT, is not necessary for cyst development at least in this model. These findings in *Pkd1* mice may also yield insights into the segmental origin of cysts in human ADPKD. In the developing human kidney, high *PKD1* expression first appears in differentiated PT starting from their glomerular origin and later in the distal nephron and the ureteric bud branches [4]. Glomerular cysts have been reported in patients with ADPKD [33], including in a severe childhood case associated with a *PKD1* deletion [34]. Earlier analyses of cyst fluid composition, electric properties and immunoreactivity for segmental markers (including AQP1 and aminopeptidase) have identified a significant number of cysts of PT origin co-existing with collecting duct cysts in end-stage kidneys of ADPKD patients [3,35].

In conclusion, we show that the deletion of polycystin-1 in this mouse model is reflected by polyhydramnios and a massive loss of solutes, including cAMP, in the AF. These changes precede the development of renal cysts, first detected in glomeruli and PT. These features give insights into the role of polycystin-1 in renal development, the mechanisms of cystogenesis and the tubular alterations encountered in ADPKD.

Supplementary data

Supplementary data are available online at http://ndt.oxfordjournals.org

Conflict of interest statement. None declared.

References

1. Pirson Y, Chauveau D, Devuyst O. Autosomal dominant polycystic kidney disease. *Oxford Textbook of Clinical Nephrology.* Oxford: Oxford University Press, 2005; 3rd Edition, 2304–2324
2. Torres VE, Harris PC. Mechanisms of disease: autosomal dominant and recessive polycystic kidney diseases. *Nature Clin Prac Neph* 2006; 2: 40–55
3. Devuyst O, Beauwens R. Ion transport and cystogenesis: the paradigm of autosomal dominant polycystic kidney disease. *Advances in Nephrology.* St. Louis: Mosby, 1998; 28439–478
4. Chauvet V, Qian F, Boute N *et al.* Expression of PKD1 and PKD2 transcripts and proteins in human embryo and during normal kidney development. *Am J Pathol* 2002; 160: 973–983
5. Boulter C, Mulroy S, Webb S *et al.* Cardiovascular, skeletal, and renal defects in mice with a targeted disruption of the Pkd1 gene. *Proc Natl Acad Sci USA* 2001; 98: 12174–12179

6. Lu W, Peissel B, Babakhanlou H *et al*. Perinatal lethality with kidney and pancreas defects in mice with a targetted Pkd1 mutation. *Nat Genet* 1997; 17: 179–181

7. Kim K, Drummond I, Ibraghimov-Beskrovnaya O *et al*. Polycystin 1 is required for the structural integrity of blood vessels. *Proc Natl Acad Sci USA* 2000; 97: 1731–1736

8. Lu W, Shen X, Pavlova A *et al*. Comparison of Pkd1-targeted mutants reveals that loss of polycystin-1 causes cystogenesis and bone defects. *Hum Mol Genet* 2001; 10: 2385–2396

9. Muto S, Aiba A, Saito Y *et al*. Pioglitazone improves the phenotype and molecular defects of a targeted Pkd1 mutant. *Hum Mol Genet* 2002; 11: 1731–1742

10. Nishio S, Hatano M, Nagata M *et al*. Pkd1 regulates immortalized proliferation of renal tubular epithelial cells through p53 induction and JNK activation. *J Clin Invest* 2005; 115: 910–918

11. Casal JA, Hermida J, Lens XM *et al*. A comparative study of three kidney biomarker tests in autosomal dominant polycystic kidney disease. *Kidney Int* 2005; 68: 948–954

12. Allen E, Piontek KB, Garrett-Mayer E *et al*. Loss of polycystin-1 or polycystin-2 results in dysregulated apolipoprotein expression in murine tissues via alterations in nuclear hormone receptors. *Hum Mol Genet* 2006; 15: 11–21

13. Ahrabi AK, Terryn S, Valenti G *et al*. Pkd1 haploinsufficiency causes a syndrome of inappropriate antidiuresis in mouse. *J Am Soc Nephrol* 2007; 18: 1740–1753

14. Ibraghimov-Beskrovnaya O, Dackowski WR, Let F *et al*. Polycystin: in vitro synthesis, in vivo tissue expression, and subcellular localization identifies a large membrane-associated protein. *Proc Natl Acad Sci USA* 1997; 94: 6397–6402

15. Halatek T, Hermans C, Broeckaert F *et al*. Quantification of Clara cell protein in rat and mouse biological fluids using a sensitive immunoassay. *Eur Respir J* 1998; 11: 726–733

16. Christensen EI, Brin H. Megalin and cubilin: multifunctional endocytic receptors. *Nat Rev Mol Cell Biol* 2002; 3: 256–266

17. Murata F, Tsuyama S, Suzuki S *et al*. Distribution of glycoconjugates in the kidney studied by use of labelled lectins. *J Histochem Cytochem* 1983; 31: 139–144

18. Guillaume R, D'Agati V, Daoust M *et al*. Murine Pkd1 is a developmentally regulated gene from morula to adulthood: role in tissue condensation and patterning. *Dev Dyn* 1999; 214: 337–348

19. Pritchard L, Sloane-Stanley JA, Sharpe JA *et al*. A human PKD1 transgene generates functional polycystin-1 in mice and is associated with a cystic phenotype. *Hum Mol Genet* 2000; 9: 2617–2627

20. Thivierge C, Kurbegovic A, Couillard M *et al*. Overexpression of PKD1 causes polycystic kidney disease. *Mol Cell Biol* 2006; 26: 1538–1548

21. Brace RA, Wolf EJ. Normal amniotic fluid volume changes throughout pregnancy. *Am J Obstet Gynecol* 1989; 161: 382–389

22. Cheung CY, Brace RA. Amniotic fluid volume and composition in mouse pregnancy. *J Soc Gynecol Investig* 2005; 12: 558–562

23. Kirshon B. Fetal urine in hydramnios. *Obstet Gynecol* 1989; 73: 240–242

24. Jouret F, Igarashi T, Gofflot F *et al*. Comparative ontogeny, processing, and segmental distribution of the renal chloride channel, ClC-5. *Kidney Int* 2004; 65: 198–208

25. Loughna S, Landels E, Woolf AS. Growth factor control of developing kidney endothelial cells. *Exp Nephrol* 1996; 4: 112–118

26. Yuen BH, Wittmann B, Staley K. Cyclic adenosine 3', 5'-monophosphate (cAMP) in pregnancy body fluids during normal and abnormal pregnancy. *Am J Obstet Gynecol* 1976; 125: 597–602

27. Webster SK, Haramati A. Developmental changes in the phosphaturic response to parathyroid hormone in the rat. *Am J Physiol* 1985; 249: F251–F255

28. Gattone VH, Xiaofang W, Harris PC *et al*. Inhibition of renal cystic disease development and progression by a vasopressin V2 receptor antagonist. *Nature Medicine* 2003; 9: 1323–1326

29. Torres VE, Xiaofang W, Qian Q *et al*. Effective treatment of an orthologous model of autosomal dominant polycystic kidney disease. *Nature Medicine* 2004; 10: 363–364

30. Wang X, Gattone V 2nd, Harris PC *et al*. Effectiveness of vasopressin V2 receptor antagonists OPC-31260 and OPC-41061 on polycystic kidney disease development in the PCK rat. *J Am Soc Nephrol* 2005; 16: 846–851

31. Magenheimer BS, St John PL, Isom KS *et al*. Early embryonic renal tubules of wild-type and polycystic kidney disease kidneys respond to cAMP stimulation with cystic fibrosis transmembrane conductance regulator/Na+, K+, 2Cl– co-transporter-dependent cystic dilation. *J Am Soc Nephrol* 2006; 17: 3424–3437

32. Torres VE, Bankir L, Grantham JJ. A case for water in the treatment of polycystic kidney disease. *Clin J Am Soc Nephrol* 2009; 4: 1140–1150

33. Verani RR, Silva FG. Histogenesis of the renal cysts in adult (autosomal dominant) polycystic kidney disease: a histochemical study. *Mod Pathol* 1988; 1: 457–463

34. Torra R, Badenas C, Darnell A *et al*. Autosomal dominant polycystic kidney disease with anticipation and Caroli's disease associated with a PKD1 mutation. *Kidney Int* 1997; 52: 33–38

35. Devuyst O, Burrow CR, Smith BL *et al*. Expression of aquaporins-1 and -2 during nephrogenesis and in autosomal dominant polycystic kidney disease. *Am J Physiol* 1996; 271: F169–F183

HPMCs INDUCE GREATER INTERCELLULAR DELOCALIZATION OF TIGHT JUNCTION-ASSOCIATED PROTEINS DUE TO A HIGHER SUSCEPTIBILITY TO H_2O_2 COMPARED WITH HUVECs

Takashi Horiuchi,[1] Kazuya Matsunaga,[1] Masatoshi Banno,[1] Yusuke Nakano,[1] Kohei Nishimura,[1] Chika Hanzawa,[1] Kei-ichi Miyamoto,[1] Shinsuke Nomura,[2] and Yuji Ohta[3]

Division of Chemistry for Materials,[1] Faculty of Engineering, Graduate School of Mie University; Division of Therapeutic Blood Purification,[2] Mie University School of Medicine, Ochanomizu University,[3] Tsu, Mie, Japan

♦ Background: Reactive oxygen species (ROS) have been speculated as possible inducers of structural or functional changes that lead to a hyperpermeable state in patients on long-term peritoneal dialysis. This study aimed to compare localization of tight junction-associated proteins (TJPs), which relate to solute permeability characteristics, between human peritoneal mesothelial cell (HPMC) monolayers and human umbilical vein endothelial cell (HUVEC) monolayers under oxidative stress.
♦ Methods: HPMCs and HUVECs were cultured on a polymer mesh until transepithelial electrical resistance reached a plateau. Solute permeation tests were conducted using FITC-labeled dextrans. Localization of TJPs was observed under a confocal laser scanning microscope. These experiments were carried out with/without 0.1 mmol/L H_2O_2. In addition, ROS production as well as the amounts of intracellular reductive glutathione (GSH) and oxidative glutathione were measured.
♦ Results: When the monolayers were exposed to 0.1 mmol/L H_2O_2/medium for 2 hours, the HPMC monolayer revealed a significant reduction in transepithelial electrical resistance (from 32.5 ± 3.4 to 17.4 ± 4.9 $\Omega \cdot cm^2$) with delocalization of TJPs, particularly occludins. The HUVEC monolayer remained stable and exhibited an unremarkable change in TJP organization. Compared to the HUVEC monolayer, the HPMC monolayer exhibited two- to threefold higher 2′,7′-dichlorofluorescein intensities that increased in a dose-dependent manner. HUVECs contained approximately 2.5-times more GSH than HPMCs. This supported the lesser production of ROS when exposed to 0.1 mmol/L H_2O_2 for 24 hours. HUVECs used 8.03 nmol/mg GSH protein to maintain TJP localization, while only 3.75 nmol/mg GSH protein was available for the HPMCs.
♦ Conclusion: The HUVEC monolayer, which was less permeable to middle-to-high molecular weight solutes, was more tolerant against ROS stress than the HPMC monolayer.

Correspondence to: T. Horiuchi, Division of Chemistry for Materials, Faculty of Engineering, Graduate School of Mie University, 1577 Kurima-Machiyacho, Tsu, Mie, 514-8507 Japan.
horiuchi@chem.mie-u.ac.jp

Availability of intracellular GSH is an important issue in maintaining the integrity of the mesothelium.

Solute and water transport via the peritoneum, which is composed of the mesothelium and the interstitium embedding a network of capillaries, is a major principle of continuous ambulatory peritoneal dialysis therapy. This complex structure, however, hinders our efforts to find the most critical region in the peritoneum when a patient has an unsatisfactory outcome, such as insufficient water and solute removal.

To assess the functional integrity of the peritoneum, the three-pore model developed by Rippe and Stelin has been clinically utilized as the most informative analytical tool (1). In this model, solute permeation data are fitted to theoretical equations on the basis of three hypothetical pores. Although an ultrasmall pore with estimated diameter of 4 – 6 Å has been hypothesized as the water transport channel (*i.e.*, aquaporins), the morphologically corresponding pathways for the other two pores (*i.e.*, small pores and large pores) have not yet been satisfactorily determined.

In the peritoneal equilibration test (PET) commonly used clinically, water soluble substances with low molecular weight, such as creatinine and urea, are monitored and evaluated as dialysate-to-plasma (D/P) ratios (2). Although change in effective peritoneal surface area is one of the crucial factors influencing the D/P ratio, the more intrinsic property, namely solute permeability, should be discussed. Which pathway in the three-pore model would correspond to D/P ratio in a PET? Small

217

pores would be responsible for this pathway because their estimated pore size is around 40 Å. Moreover, the intercellular pathway (lateral) could be specified because these substances do not have a specific transport channel on the plasma membrane.

In the cellular physiology of epithelium and endothelium, an intracellular junction apparatus has been noted as a solute transport barrier, in particular the tight junction (TJ) located at the most apical position (3–5). The role of the TJ as a solute transport barrier differs in different types of cells. For example, higher solute transport barrier is noted in the vascular endothelial cells of the brain aortic capillary and the cornea (6,7), and in the epithelial cells of the bowel and the cornea (8,9). Our previous study, wherein we constructed a human peritoneal mesothelial cell (HPMC) monolayer on a polymer mesh, suggested the existence of a solute transport barrier that was also controlled by tight junction-associated proteins (TJPs) (10). These TJP organizations relate to epithelial-to-mesenchymal transition in which transforming growth factor-beta1 (TGF-β1) downregulates E-cadherin through expression of transcriptional factor Snail (11). It has been reported that Snail modulates TJPs of Madin–Darby canine kidney cells, resulting in increased ion permeability (12). As described elsewhere, TGF-β1 is not the only factor, other factors such as reactive oxygen species (ROS) and advanced glycated end products may be involved in this cellular event (13,14).

Based on this evidence, we hypothesized that TJ characteristics, which relate to solute permeability and epithelial-to-mesenchymal transition, differ between peritoneal resident cells (*e.g.*, the mesothelium and the endothelium). In order to understand the mechanism of solute transport via the peritoneum and its correlation to TJP organization, it is worthwhile to characterize both the HPMC monolayer and the human umbilical vein endothelial cell (HUVEC) monolayer in the same experimental setting. The specific purposes of the present study were to compare (1) solute permeability, (2) susceptibility of TJP organization to oxidative stress, (3) ROS productivity, and (4) antioxidative capacity between HPMCs and HUVECs.

MATERIALS AND METHODS

SOURCES OF HPMCs AND HUVECs

The HPMCs were isolated by enzymatic digestion of human omentum. Omental specimens were taken from patients undergoing abdominal surgery after obtaining their consent; this procedure was approved by the Ethics Committee of Mie University Hospital (No. 369). The

HPMC cultures were established using a previously described method (15). The HUVECs were purchased from Sanko Junyaku, Tokyo, Japan, and cultured using EGM-2 medium (Cambrex, Walkersville, MD, USA). The chemicals and tissue culture plastics used in the study were described in our earlier study (16). All chemicals used in this study were purchased from Sigma-Aldrich (Tokyo, Japan), unless otherwise stated.

CONSTRUCTION OF HPMC AND HUVEC MONOLAYERS ON A MEMBRANE SUPPORT

To construct an *in vitro* model of the HPMC and HUVEC monolayers, a cell suspension (5×10^4 cells/cm^2) was seeded and cultured on a polyester mesh (Transwell, 0.4 μm pore size, 12-well type; Costar, MA, USA) using 10% fetal bovine serum (FBS)/medium. The inner and outer chambers were filled with 0.5 mL and 1.5 mL culture medium respectively; the culture medium was replaced every 3 days. In all the experiments described below, HPMCs were used within three passages.

MEASUREMENT OF TRANSEPITHELIAL ELECTRICAL RESISTANCE

Transepithelial electrical resistance (TER) was measured daily or every 2 days using an EVOM volt ohm meter with STX-2 electrodes (World Precision Instruments, Sarasota, FL, USA). The electrodes were inserted into both ends of the mesh. Alternating current of less than ±20 μA was applied between the electrodes at a frequency of 12.5 Hz. Prior to measurement, the culture medium was replaced with fresh medium (0.1% FBS/medium) and maintained at 37°C. The resistance of each monolayer was multiplied by the effective surface area to obtain the electrical resistance of that monolayer (in $\Omega \cdot cm^2$). To calculate the normalized TER of each monolayer, background TER of a blank polyester mesh was subtracted from the TER of the respective cell monolayer. Any study using the monolayer was conducted 2 days, but not more than 3 days, after steady state was achieved.

SOLUTE PERMEABILITY TEST (SPT)

Once stable TERs were obtained, the permeabilities of the HPMC and HUVEC monolayers were determined by measuring changes in the concentrations of molecular markers. Fluorescein isothiocyanate (FITC)-labeled dextrans (molecular weights 4, 10, and 70 kDa) were used as fluorescent molecular markers. Each FITC-labeled dextran was added to the inner chamber of the chamber at a final concentration of 50 μg/mL. An equimolar amount of unlabeled dextran was added to the outer chamber of

218

the polyester mesh system to maintain an isotonic condition. At 2 hours and 4 hours after the addition of a molecular marker, a 10-μL volume of each sample was collected from both sides of the chamber. Each sample was assessed using a fluorescence spectrophotometer (F-2000; Hitachi, Tokyo, Japan) at an excitation wavelength of 490 nm and an emission wavelength of 520 nm. The solute permeability coefficient (SPC), which is the flux of FITC-labeled dextran across the monolayer, was calculated using the following equation:

$$K = -\frac{4\bar{V}}{\Delta t \cdot A} \ln\left(\frac{C_{a0} - 4C_{b4}}{C_{a0} - 4C_{b2}}\right),$$

where K is the SPC (m/s), V is the volume of the basal side (m^3), A is the membrane area (m^2), Δt is the time interval (s), and C is the concentration of the molecular marker (C_{a0} = concentration at the apical side at time 0; C_{b4} = concentration at the basal side at 4 hours; C_{b2} = concentration at the basal side at 2 hours).

IMMUNOHISTOCHEMICAL STAINING OF OCCLUDINS AND ZONULA OCCLUDENS-1 (ZO-1)

Occludins and ZO-1 were immunohistochemically stained in accordance with a previously described protocol (17). Briefly, HPMCs and HUVECs were cultured on an eight-chambered slide (Nunc, NY, USA) coated with types I and III collagen (Cellmatrix Type 1-A; Nitta Gelatin, Osaka, Japan). Following confluence, HPMCs were washed twice with phosphate-buffered saline (PBS). The medium was replaced with fresh medium (0.1% FBS/M199 for HPMCs and 0.1% FBS/EGM-2 for HUVECs) and the cells were incubated for another 24 hours. Subsequently, the cells were washed twice with PBS and then cultured for 30 minutes in the test media. The cells were then fixed in cold acetone/methanol at –20°C for 5 minutes, rehydrated in PBS, and blocked for 1 hour in PBS containing 20% Block Ace (Dainippon Seiyaku, Tokyo, Japan). This was followed by overnight incubation with a primary antibody at 4°C. A rabbit anti-ZO-1 antibody (Zymed Laboratories, San Francisco, CA, USA) and a rabbit anti-occludin antibody (Zymed) were used as primary antibodies at a dilution of 1:100 and 1:50 respectively. After incubation with the primary antibody, the cells were washed 5 times with PBS. Subsequently, an appropriate secondary antibody was applied for 1 hour at room temperature, following which the cells were again washed 5 times with PBS. Polyclonal swine anti-rabbit FITC-labeled immunoglobulins (Dako, Glostrup, Denmark) were used at a dilution of 1:100 and incubated at room temperature for 1 hour. Stained specimens were examined under a confocal laser scanning microscope (Fluoview FV1000; Olympus, Tokyo, Japan).

EXOGENOUS H$_2$O$_2$ SUPPLEMENTATION INTO THE HPMC AND HUVEC MONOLAYERS

To examine the effect of H$_2$O$_2$ on solute permeation and TJP localization, the HMPC and HUVEC monolayers were supplemented with exogenous H$_2$O$_2$. Prior to the SPT, the effect of H$_2$O$_2$ on enzymatic activities of mitochondria was assessed in a dose-dependent manner using the 3-(4,5-dimethylthiazol-2-yl)-2,5-diphenyltetrazolium bromide (MTT) assay, which is an indicator of the activity of mitochondrial dehydrogenases. The H$_2$O$_2$ was applied at final concentrations of 0.05, 0.1, 0.5, and 1.0 mmol/L and exposure time was set at 2 hours.

For the SPT, 0.1 and 1.0 mmol/L were selected as H$_2$O$_2$ concentrations based on the results of the MTT assay. After 30-minutes' exposure of the HPMC and HUVEC monolayers to 0.1 mmol/L and 1.0 mmol/L H$_2$O$_2$/medium, SPTs were performed according to the protocol described above.

Immunohistochemical examinations were also carried out to assess the effect of H$_2$O$_2$ on TJP delocalization.

OBSERVATION OF INTRACELLULAR ROS PRODUCTION USING 2′,7′-DICHLOROFLUORESCEIN DIACETATE (DCFH-DA)

To quantify intracellular ROS production, DCFH-DA (Sigma, Japan), a fluorescence probe that permeates the cell membrane, was added to the HPMC and HUVEC monolayers at a final concentration of 10 μmol/L after 15 minutes' incubation with 0.01, 0.1, and 1.0 mmol/L H$_2$O$_2$/medium. DCFH-DA was allowed to incorporate into the cells for 15 minutes at 37°C; DCF produced as a result of ROS-induced DCFH oxidation was detected under a confocal laser scanning microscope at an excitation wavelength of 480 nm and an emission wavelength of 530 nm (18).

MEASUREMENTS OF INTRACELLULAR REDUCTIVE GLUTATHIONE (GSH) AND OXIDATIVE GLUTATHIONE (GLUTATHIONE DISULFIDE; GSSG)

The amounts of intracellular GSH and GSSG were measured using an enzymatic recycling method (19). Briefly, after discarding the culture medium, the monolayer cultured on a 35-mm diameter culture flask was washed twice with PBS. The scraped cells were resuspended in 80 μL 10 mmol/L HCl and then frozen at –80°C for 15 minutes. Thawing and freezing of the cell suspension was repeated a couple of times following

219

deproteinization with 5% sulfosalicylic acid. Supernatant (20 μL) was added to a mixture of 30 μL glutathione reductase and 20 μL of 1 mmol/L NADPH. After incubation for 10 minutes at 37°C, 20 μL 10 mmol/L DTNB was added and absorbance was measured at 405 nm at a certain time interval.

To measure the amount of GSSG, 2-vinylpyridine was added prior to the above-mentioned GSH measurement because 2-vinylpyridine inhibits the reduction of GSSG to GSH by binding to GSSG. Therefore, the amount of GSSG could be calculated by subtracting the GSH amount from the total glutathione amount.

DATA ANALYSIS

All data are expressed as mean ± SD. Statistical significance of TER, MTT, and solute permeabilities were calculated using Student's t-test. The level of significance was set at $p < 0.05$. For the analysis of covariance, we used SAS software for statistical analysis (SAS/STAT User's Guide Release, 6.03 Edition; Tokyo, Japan).

RESULTS

TRANSEPITHELIAL ELECTRICAL RESISTANCES AND SPCs UNDER PHYSIOLOGICAL CONDITIONS

As shown in Figure 1, the normalized TER increased steadily, beginning at 0 and leveling off at 23.7 ±
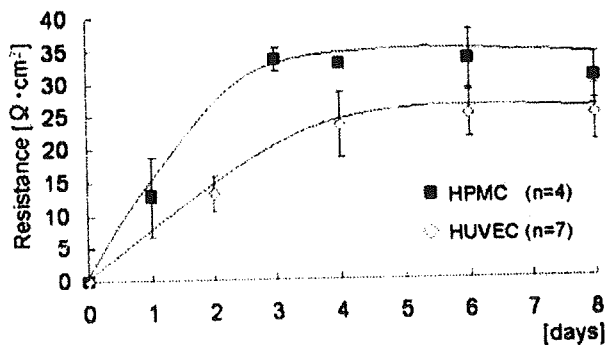
Figure 1 — Comparison of the transepithelial resistances (TERs) between human peritoneal mesothelial cell (HPMC) and human umbilical vein endothelial cell (HUVEC) monolayers. Development of TER in HPMC and HUVEC monolayers cultured on a polyester membrane support (pore size 0.4 μm) was observed. The normalized TER, which was obtained by subtracting the background TER of the blank polyester membrane support from the calculated TER, increased steadily, beginning at 0 and leveling off at 23.7 ± 3.2 Ω·cm² on the eighth day ($n = 7$) for the endothelial monolayer and at 32.3 ± 2.8 Ω·cm² on the fifth day ($n = 4$) for the mesothelial monolayer.

3.2 Ω·cm² on the eighth day ($n = 7$) for the endothelial monolayer, and at 32.3 ± 2.8 Ω·cm² on the fifth day ($n = 4$) for the mesothelial monolayer (10). This was accompanied by confluence of cells, as previously mentioned.

As distinctly seen in Figure 2, solute permeability of the HUVEC monolayer on the polymer mesh was lower than that of the HPMC monolayer, indicating that the HUVEC monolayer is more resistant to permeation by middle and high molecular weight solutes. A real SPC (K_{real}) was calculated by subtracting the blank SPC from the measured SPC in an inverse fashion:

$$1/K_{real} = 1/K_{measured} - 1/K_{blank}.$$

$K_{real,HPMC}$ for 70-, 10-, and 4-kDa dextrans was approximately 8, 3, and 2 times higher than that of $K_{real,HUVEC}$, respectively (Figure 3).

TRANSEPITHELIAL ELECTRICAL RESISTANCES AND SPCs UNDER OXIDATIVE CONDITIONS

Prior to the experiments conducted using H_2O_2, enzymatic activities of mitochondria were evaluated by the MTT assay wherein both HPMCs and HUVECs were exposed to varying concentrations of H_2O_2 for 2 hours. There were no significant changes in MTT values during 2 hours of exposure to 0.1 mmol/L H_2O_2 for HPMCs and HUVECs (Figure 4).

The normalized TER of the HPMC monolayer reduced gradually (from 32.5 ± 3.4 to 17.4 ± 4.9 Ω·cm²) during the 2-hour exposure to 0.1 mmol/L H_2O_2/M199 ($n = 7$).
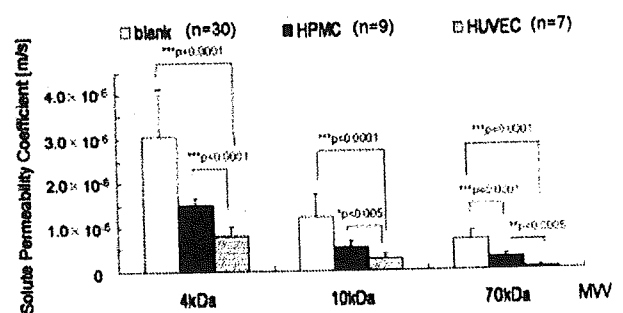

Figure 2 — Comparison of solute permeability coefficients (SPCs) between human peritoneal mesothelial cell (HPMC) and human umbilical vein endothelial cell (HUVEC) monolayers. The SPCs of the polymer mesh (pore size 0.4 μm) for each molecular marker with and without the HPMC and HUVEC monolayers were measured. As seen in the figure, the solute permeability of the HUVEC monolayer on the polymer mesh was lower than that of the HPMC monolayer, indicating that the HUVEC monolayer is more resistant to the permeation of middle and high molecular weight solutes.
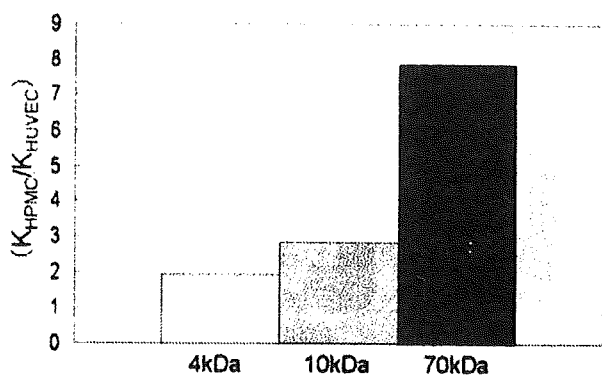
Figure 3 — Comparison of real solute permeability coefficients (SPCs; K_{real}). $K_{real,HPMC}$ for 70-, 10-, and 4-kDa dextrans were approximately 8, 3, and 2 times higher than the corresponding $K_{real,HUVEC}$. Real SPCs (K_{real}) were calculated by subtracting the blank SPC from the measured SPC in an inverse fashion: $1/K_{real} = 1/K_{measured} - 1/K_{blank}$. HPMC = human peritoneal mesothelial cell; HUVEC = human umbilical vein endothelial cell.
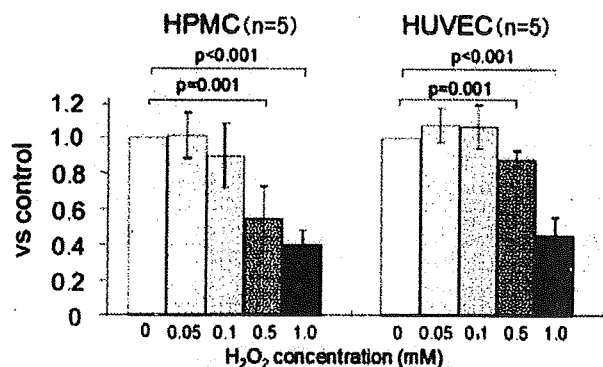

Figure 4 — Effect of supplemented H_2O_2 concentration on the viability of human peritoneal mesothelial cells (HPMCs) and human umbilical vein endothelial cells (HUVECs). Enzymatic activities of mitochondria were evaluated by 3-(4,5-dimethylthiazol-2-yl)-2,5-diphenyl tetrazolium bromide (MTT) assay. HPMCs and HUVECs were exposed to various concentrations of H_2O_2 for 2 hours. A marked reduction in cell viability was seen for >0.5 mmol/L H_2O_2.

On the other hand, there was no significant reduction in the TER of the HUVEC monolayer during the 2-hour exposure to 0.1 mmol/L H_2O_2/EGM-2 ($n = 9$), as shown in Figure 5.

Figure 6 shows the SPCs of the polymer mesh (pore size 0.4 μm) for each molecular marker with and without the HPMC and HUVEC monolayers. As distinctly seen in the figure, the solute permeability of the HUVEC monolayer on the polymer mesh was lower than that of the HPMC monolayer, indicating that the HUVEC monolayer is more resistant to the permeation of middle and high molecular weight solutes.
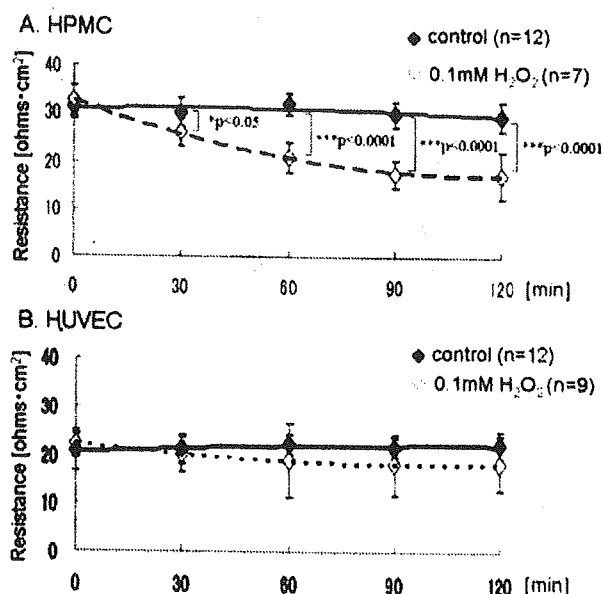

Figure 5 — Comparison between the human peritoneal mesothelial cell (HPMC) and human umbilical vein endothelial cell (HUVEC) monolayers with respect to changes in transepithelial resistance (TER) due to exposure to 0.1 mmol/L H_2O_2. Changes in TER of HPMC (A) and HUVEC (B) monolayers due to exposure to 0.1 mmol/L H_2O_2 were recorded. The normalized TER of the HPMC monolayer reduced gradually, from 32.5 ± 3.4 to 17.4 ± 4.9 $\Omega \cdot cm^2$ during 2-hours of exposure to 0.1 mmol/L H_2O_2/ M199 ($n = 7$). On the other hand, there was no significant reduction in TER of the HUVEC monolayer during 2-hours of exposure to 0.1 mmol/L H_2O_2/EGM-2 ($n = 9$).

INTERCELLULAR LOCALIZATION OF OCCLUDINS AND ZO-1 UNDER OXIDATIVE CONDITIONS

Immunohistochemical staining of occludins and ZO-1 clearly showed the intercellular localization of TJPs. In the control, TJPs, occludins, and ZO-1 were localized along the intercellular spaces, as shown in the left panels of Figure 7. On the other hand, the localized occludins diminished from the intercellular space when the HPMC monolayer was exposed to 0.1 mmol/L H_2O_2, while they were maintained in the HUVEC monolayer. Disappearance of localized ZO-1 was also observed; however, ZO-1 disappeared to a lesser extent than the occludins.

INTRACELLULAR PRODUCTION OF ROS UNDER OXIDATIVE CONDITIONS

Figure 8 clearly indicates the dose-dependent production of ROS in both HPMC and HUVEC monolayers due to exposure to 0.1 mmol/L H_2O_2. A higher production was observed in the HPMC monolayer than in the HUVEC monolayer, even without H_2O_2 exposure.
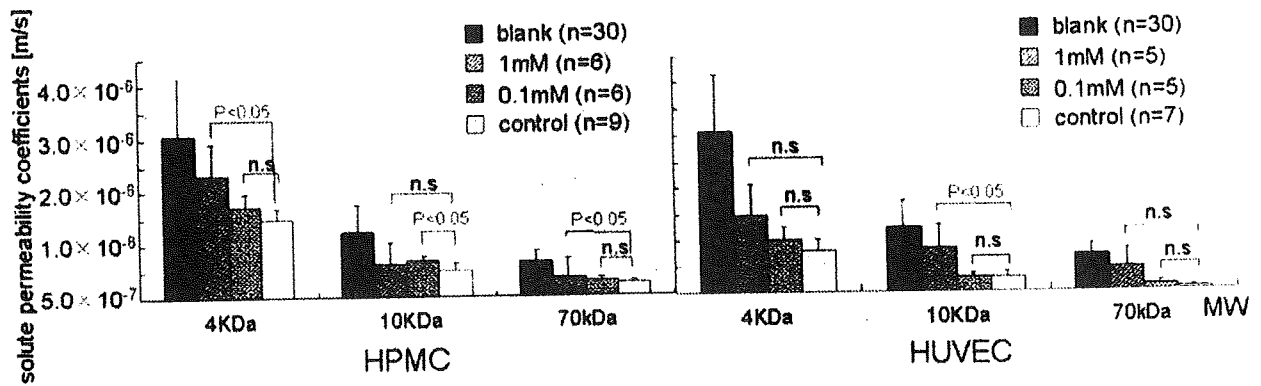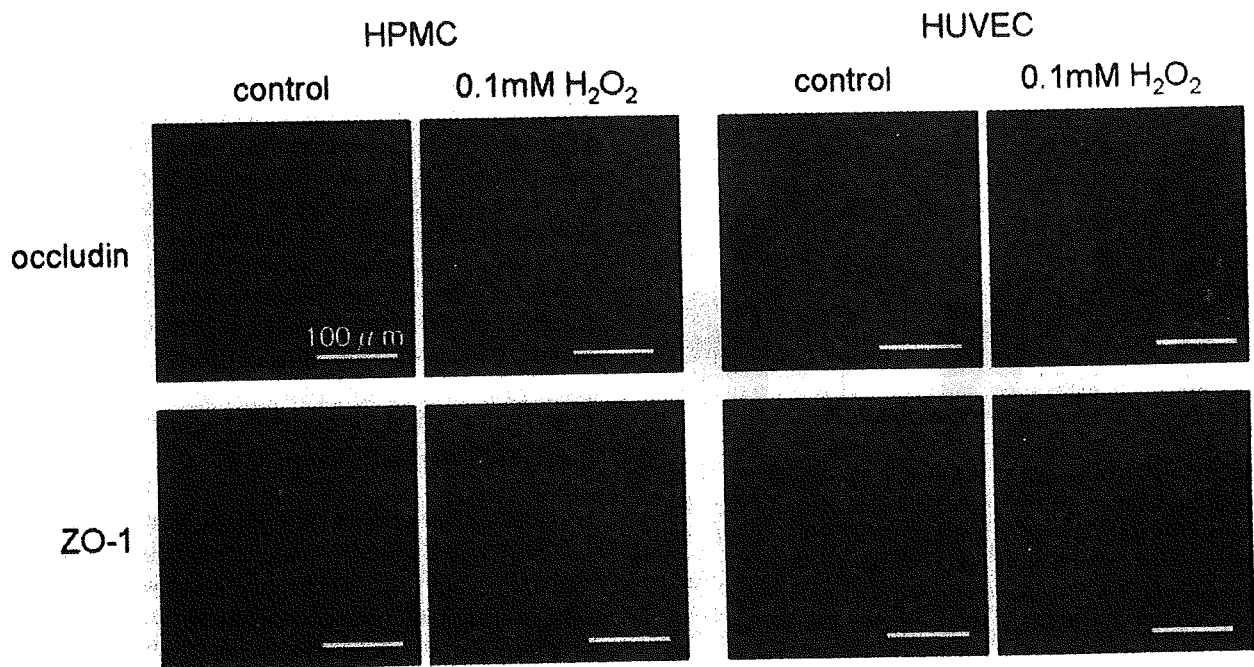
221

Figure 6 — Comparison between human peritoneal mesothelial cell (HPMC) and human umbilical vein endothelial cell (HUVEC) monolayers with respect to changes in solute permeability coefficients (SPCs) due to exposure to H_2O_2. The SPCs of the HPMC and HUVEC monolayers due to exposure to H_2O_2 were measured after 30 minutes of exposure to H_2O_2. There was no significant change in the SPCs of any of the dextrans through either monolayer except for changes in the 10-kDa dextran through the HPMC monolayer when H_2O_2 was supplemented at a final concentration of 0.1 mmol/L.

Figure 7 — Comparison between the human peritoneal mesothelial cell (HPMC) and human umbilical vein endothelial cell (HUVEC) monolayers with respect to the intercellular localization of occludins and zonula occludens-1 (ZO-1) due to exposure to 0.1 mmol/L H_2O_2. Immunohistochemical staining of occludins and ZO-1 clearly show the intercellular localization of these tight junction-associated proteins (TJPs). In the control, TJPs, occludins, and ZO-1 were localized along the intercellular spaces, as shown in the left panels. On the other hand, localized occludins diminished from the intercellular space when the cells were supplemented with 0.1 mmol/L H_2O_2. Disappearance of localized ZO-1 was also observed; however, ZO-1 disappeared to a lesser extent than occludins.

AMOUNT OF INTRACELLULAR GSH AND GSSG WITH/WITHOUT 24-HOUR EXPOSURE TO 0.1 MMOL/L H_2O_2

   The amount of total glutathione per milligram proteins was significantly greater in HUVECs than in HPMCs (23.4 ± 11.7 vs 7.19 ± 3.74 nmol/mg protein) (Figure 9).

Due to the 24-hour exposure to 0.1 mmol/L H_2O_2, the amount of GSH decreased significantly, from 12.2 ± 8.67 to 4.17 ± 0.98 nmol/mg protein in the HUVECs and from 4.83 ± 3.10 to 1.08 ± 0.51 nmol/mg protein in the HPMCs. There was no significant change in the amount of total glutathione in either HPMCs or HUVECs.

222

DISCUSSION

SOLUTE TRANSPORT THROUGH CULTURED MONOLAYER UNDER PHYSIOLOGICAL CONDITIONS

To evaluate the integrity of the cellular junctions, we employed the measurement of TER at a low frequency (12.5 Hz), which represents the resistance of passive electrolyte motion through the paracellular pathways. The approximately 1.4-times higher TER of the HPMC monolayer in our experiments is consistent with the reference values summarized in our previous paper (10). Based on these data, we estimated the same tendency for the SPCs of the marker solutes, that is, lower solute permeability for the HPMC monolayer than the HUVEC monolayer.

For the endothelial monolayer, the SPC of D-70 (3.8 × 10^{-6} cm/s) was almost similar to the values of albumin

$(4.5 - 5.6 \times 10^{-6}$ cm/s) and dextran $(3 - 8 \times 10^{-6}$ cm/s) reported previously (10). As can be seen in Figure 3, the real SPC of D-70 for the HPMC monolayer was approxi-
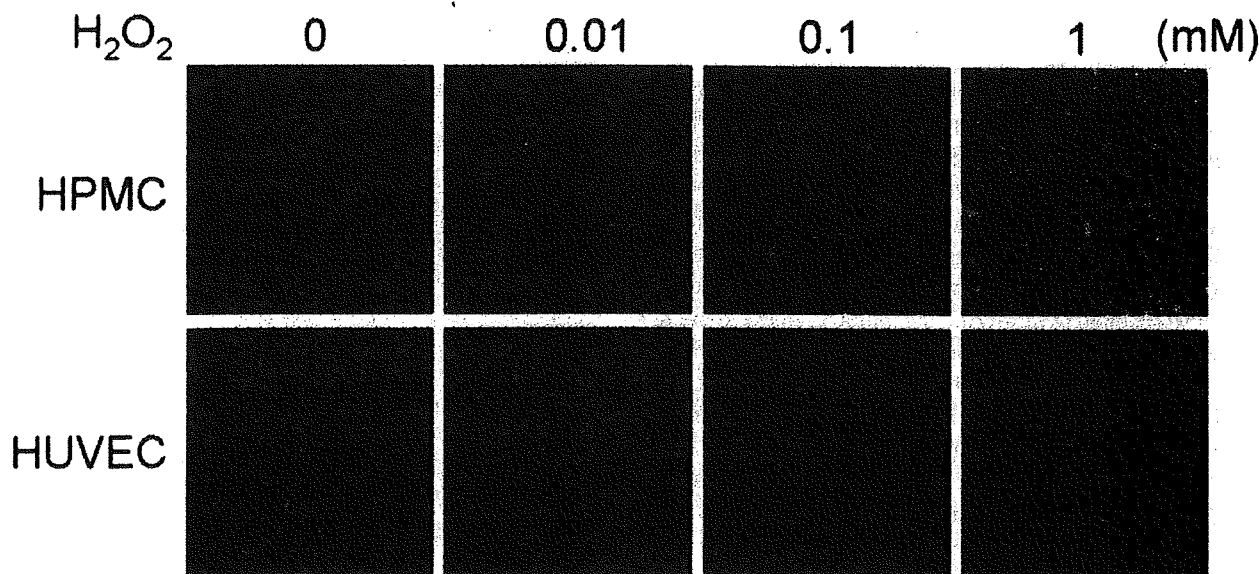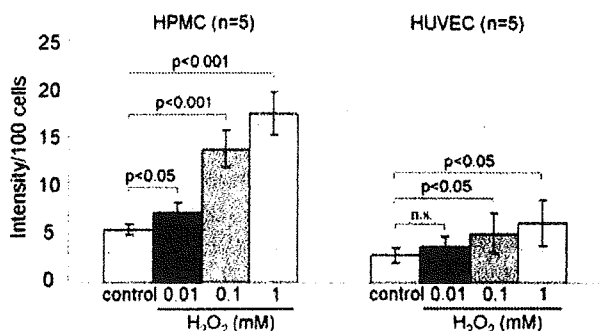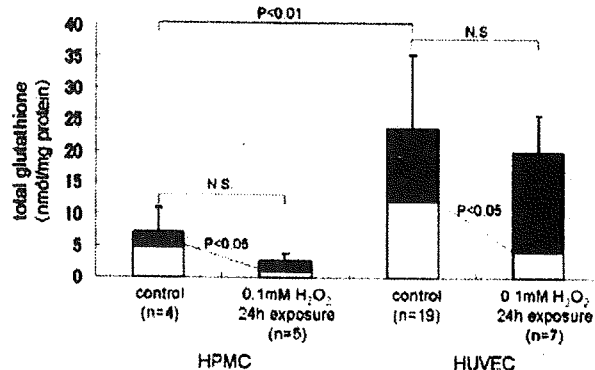
Figure 9 — Comparison between human peritoneal mesothelial cell (HPMC) and human umbilical vein endothelial cell (HUVEC) monolayers with respect to the amount of intracellular reductive glutathione (GSH; white bars) and oxidative glutathione (GSSG; black bars) with/without 24-hour exposure to 0.1 mmol/L H_2O_2. The amount of total glutathione per milligram proteins was significantly greater in HUVECs than in HPMCs (23.4 ± 11.7 vs 7.19 ± 3.74 nmol/mg protein). Due to this 24-hour exposure to 0.1 mmol/L H_2O_2, the amount of GSH decreased significantly, from 12.2 ± 8.67 to 4.17 ± 0.89 nmol/mg protein, in the HUVECs and from 4.83 ± 3.10 to 1.08 ± 0.51 nmol/mg protein in the HPMCs. There was no significant change in the amount of total glutathione in either HPMCs or HUVECs.

Figure 8 — Comparison between human peritoneal mesothelial cell (HPMC) and human umbilical vein endothelial cell (HUVEC) monolayers with respect to intracellular production of reactive oxygen species (ROS) due to exposure to various concentrations of H_2O_2. Dose-dependent production of ROS was observed in both HPMC and HUVEC monolayers. The HPMC monolayer exhibited higher production than the HUVEC monolayer.

223